arXiv:1211.0723v1 [physics.atom-ph] 4 Nov 2012

Cavity-aided non-demolition measurements for atom counting and spin squeezing

Zilong Chen,[*] Justin G. Bohnet, Joshua M. Weiner, Kevin C. Cox, and James K. Thompson[†]
JILA, NIST and University of Colorado, Department of Physics,
University of Colorado, Boulder, Colorado 80309, USA

(Dated: November 6, 2012)

Probing the collective spin state of an ensemble of atoms may provide a means to reduce heating via the photon recoil associated with the measurement and provide a robust, scalable route for preparing highly entangled states with spectroscopic sensitivity below the standard quantum limit for coherent spin states. The collective probing relies on obtaining a very large optical depth that can be effectively increased by placing the ensemble within an optical cavity such that the probe light passes many times through the ensemble. Here we provide fundamental expressions for such cavity-aided non-demolition measurements. We also provide experimental examples related to previous work [1] using quantum non-demolition measurements to prepare conditionally spin-squeezed states in a large ensemble of nearly 10^6 ^{87}Rb atoms. Fundamental limits on spectroscopic enhancements in ^{87}Rb are considered.

PACS numbers: 42.50.Dv, 42.50.Pq, 06.20.-f, 42.50.Lc

I. INTRODUCTION

High-resolution measurements of the populations of two-level systems are key for realizing high precision atomic sensors such as atomic clocks, magnetometers, and atom-based electric field, rotation, and inertial sensors [2]. Further, developing non-demolition, high-resolution measurement techniques to create and/or detect entangled states is a promising route to enhanced sensor precision or bandwidth [1, 3–12].

In trapped neutral atom ensembles, non-demolition measurements that do not cause atom loss from the trap could lead to significant advances in the repetition rates of sensors [13], allowing them to operate closer to the regime of ion-based sensors in which the ions can be stored over many repeated measurement cycles [14]. Furthermore, a quantum non-demolition measurement that also preserves quantum coherence can prepare conditionally spin-squeezed states with spectroscopic sensitivity below the Standard Quantum Limit (SQL) $\Delta\theta_{\rm SQL} = 1/\sqrt{N}$ that arises from the quantum projection noise of N independent atoms [15].

The results described in this work are relevant to the recently demonstrated approaches for generating entangled states in large ensembles using many diverse approaches, including quantum non-demolition measurements [1, 6, 7], one-axis twisting schemes based on cavity-mediated interactions [16], and direct collisional interactions that generate one-axis squeezing [5, 8, 9] or parametric pair generation [10, 12]. In all of these cases, a low noise readout such as the approach described in this paper is always required to actually exploit the enhanced phase-sensing properties of these states.

In particular, there has been substantial recent interest in developing non-demolition readout schemes for large laser-cooled and quantum-degenerate neutral atomic ensembles consisting of roughly 10^3 to 10^7 atoms [1, 6, 7, 11, 13, 18–20]. It is well known that significant improvements in readout sensitivity can be achieved by optically probing ensembles in free space along directions of high resonant optical depth. This approach has been extensively analyzed theoretically [21–32], and experimentally

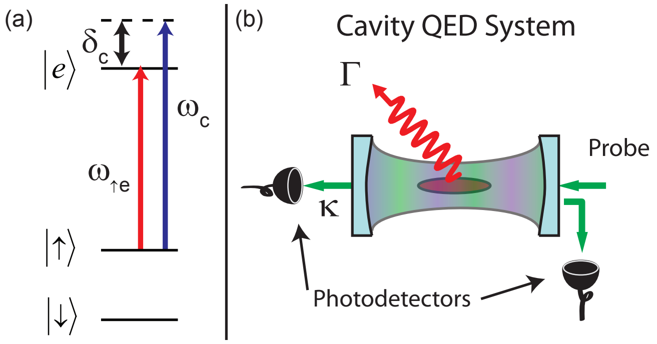

FIG. 1. (Color online) (a) Relevant energy levels. The pseudo-spin 1/2 system typically comprises two metastable states $|\uparrow\rangle, |\downarrow\rangle$, which are utilized in atomic sensors and clocks. The number of atoms $N_\uparrow$ in $|\uparrow\rangle$ modifies the cavity resonance frequency. Initially, we will assume the optically excited state $|e\rangle$ does not couple to $|\downarrow\rangle$ because of dipole selection rules or because the coupling is highly non-resonant $\delta_c \ll \omega_{\rm hf}$, where $\omega_{\rm hf}$ is the frequency separation between $|\uparrow\rangle$ and $|\downarrow\rangle$. (b) Transmitted and/or reflected probe light is monitored to determine the cavity resonance frequencies and hence the number of atoms in $|\uparrow\rangle$. An applied NMR-like microwave rotation can swap the populations between ground states so that a subsequent measurement can also determine the $|\downarrow\rangle$ population $N_\downarrow$. The ensemble of atoms are trapped in an intracavity optical lattice (blue-green). The total cavity power decay rate is κ. Single atom spontaneous decay from $|e\rangle$ at rate Γ leads to photon recoil heating and single-atom wavefunction collapse. The goal then is to extract collective information from the probe mode more rapidly than the undesired single-atom photon scattering into free space.

---

[*] zchen@jila.colorado.edu
[†] jkt@jila.colorado.edu

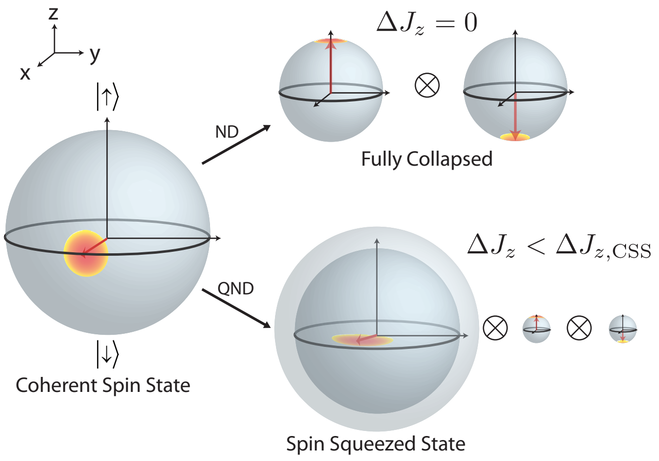

FIG. 2. (Color online) Visualization of a non-demolition (ND) (upper right) and a quantum non-demolition (QND) (lower right) measurement. A coherent spin state (CSS) for an ensemble of N spin-1/2 atoms prior to measurement is represented as a Bloch vector (red arrow) of length $N/2$. The quantum noise in the orientation of the Bloch vector is visualized as a quasi-probability distribution (red/yellow region) perpendicular to the Bloch vector, with rms opening angle at the Standard Quantum Limit (SQL) $\Delta\theta_{\mathrm{SQL}} = 1/\sqrt{N}$. A non-demolition measurement in this paper will refer to a measurement of the state's $\hat{z}$ spin projection $J_z = (N_\uparrow - N_\downarrow)/2$ with an rms imprecision $\Delta J_z < \Delta J_{z,\mathrm{CSS}} = \sqrt{N}/2$, and with the majority of the atoms remaining trapped after the measurement. For example, in the ND measurement visualized on the right, the measurement imprecision is $\Delta J_z = 0$, but after the measurement the atoms are described by a product state of atoms in spin up and down due to single-atom state information gained by the environment via free space scattering of light. We define a quantum non-demolition measurement via the additional requirement that a sufficiently large number of atoms remain in a coherent superposition of spin up and down such that the resulting state, conditioned on the measurement outcome, has a polar angle uncertainty $\Delta\theta < \Delta\theta_{\mathrm{SQL}}$. The definition of quantum non-demolition employed here is related to, but less restrictive than that of Ref. [17]. The lower right QND example visualizes the conditional state as a product state of a squeezed state and the atoms that have been collapsed into spin up and down.

studied [6, 18, 33–40].

More recently, the technique of free space probing of high optical depth samples has been extended to using optical cavities to effectively increase the optical depth of the atomic ensemble by passing the probe light through the same sample many times as shown in Fig. 1 [1, 7, 41–46]. In most of these experiments and proposals, the cavity is far-detuned from the optical transition that was probed. Probing in resonant regime [1] is an exception rather than the norm. In principle, the cavity detuning δ_c can be chosen almost arbitrarily. Therefore, a natural question to ask is: How does cavity detuning affect both the fundamental and technical atomic population measurement resolution or the degree of spin-squeezing for a given cavity geometry and cavity finesse?

To answer the question posed above, we provide detailed expressions for the fundamental scalings for probing an atomic ensemble using an optical cavity that smoothly connects the resonant to the far-detuned probing regime. We apply our results to first estimate the amount of photon-recoil heating of the ensemble when the cavity-aided measurement has an imprecision at the quantum projection noise level. The average number of photon recoils per atom sets the degree to which the measurement can be considered non-demolition. This analysis is then extended to estimate bounds on the degree of conditional spin squeezing (see Fig. 2 for details) that can be obtained using ^{87}Rb atoms in a cavity (see Fig. 1a) [1, 7]. We show that the fundamental limitations are set by the collective cooperatively parameter NC, the probe detection quantum efficiency q,and atomic properties alone. The collective cooperativity parameter NC plays a similar role to the resonant optical depth of atoms in free space, where N is the number of atoms in the probe volume and C is the single particle cooperativity parameter [47]. To illustrate these concepts we also consider technical advantages and experimental methods used in Ref. [1] for the special case that the cavity is tuned to resonance with the optically excited state.

This paper is organized as follows. In Sec. II, we begin with a review of the properties of the coupled atoms-cavity system including dissipation. This review also provides definitions and notation used throughout the paper.

In Sec. III, we derive the quantum-limited signal-to-noise ratio for non-demolition measurements of atomic populations considered as a function of the cavity detuning from atomic resonance (δ_c in Fig. 1a). We identify three different probing regimes, a resonant regime and two detuned regimes separated by a critical detuning δ_c°.

In Sec. IV, we focus on our experimental system [1], in which the atoms are probed using a cavity resonant with the atomic optically excited state $\delta_c = 0$. We include discussions of technical advantages and limitations associated with operating in this regime. Experimental details are provided for two probing schemes: a Pound-Drever-Hall type measurement and a phase-coherent demodulation of both the reflected and transmitted cavity fields into two orthogonal quadratures. We show a high degree of noise cancellation and experimentally demonstrate ac Stark shift cancellation enabled by simultaneous probing of the two resonances of the vacuum Rabi splitting.

In Sec. V, we address quantum back-action effects due to probe-induced spin flips on estimates of atomic populations in a simple three-level model. We show how the optimal measurement resolution can be achieved by balancing between noise added by spin flips and averaging down the probe's vacuum or photon shot noise.

In Sec. VI, we consider the limits set on coherence preservation. Coherence is lost due to wavefunction collapse into spin up or down driven by the same probe induced free space scattering that also causes photon recoil heating. We then obtain the optimal spectroscopic enhancement, the figure of merit for a quantum non-demolition measurement, as a function of the spin flip probability p.

In Sec. VII, we apply the results of Sec. VI to two concrete examples in ^{87}Rb: generating conditional spin squeezing first using a non-cycling optical transition, and then a cycling optical transition. Here, we demonstrate the key role of the ratio of the ground state hyperfine splitting $\omega_{\rm hf}$ to the optical transition width Γ for determining scalings and fundamental limits on conditional spin squeezing.

Finally, in Sec. VIII, we theoretically show that following a quantum non-demolition (QND) measurement near the projection noise level, a coherent re-initialization scheme can be used to reduce photon recoil heating associated with re-preparing the atomic ensemble for the next experimental cycle.

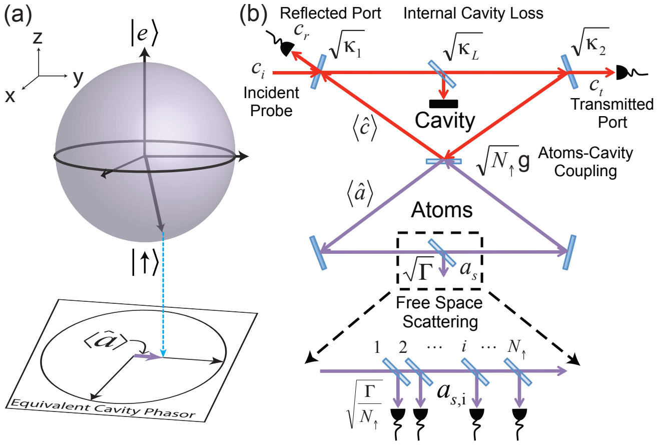

FIG. 3. (Color online) (a) Graphical representation of the linearization achieved via the Holstein-Primakoff approximation. The atomic sub-system $|\uparrow\rangle$ and $|e\rangle$ is described by a Bloch vector of length $(N_\uparrow + N_{\rm e})/2$. In the regime in which the probe light only weakly excites the atoms such that $N_{\rm e} \ll N_\uparrow$, the two-level system can be described by its projection onto a 2D plane equivalent to that describing a light field. (b) With this approximation, the collective atomic mode may be treated as an equivalent cavity mode (lower purple mode) whose coupling to the actual cavity (upper red mode) is governed by a partially reflecting mirror (center) described by a field coupling rate constant ($\sqrt{N_\uparrow} g$) that depends on the number of atoms in state $|\uparrow\rangle$. The physical mirrors have transmission coefficients described by the field coupling rates $\sqrt{\kappa_1}$ and $\sqrt{\kappa_2}$, and internal cavity losses are described by $\sqrt{\kappa_L}$, such that the total power decay rate is $\kappa = \kappa_1 + \kappa_2 + \kappa_L$. Decay of the atoms by emission of a photon into free space is described by the field transmission coefficient $\sqrt{\Gamma}$ that is the sum of the field scattering into free space modes by the atoms in $|\uparrow\rangle$. Because the scattered modes are distinguishable (expanded view of free space scattering port), it is possible to tell which atoms are in $|\uparrow\rangle$ from the free-space-scattered photons, destroying any coherent superposition between $|\uparrow\rangle$ and another state $|\downarrow\rangle$ (not shown) that may have been prepared for sensing a quantum phase.

II. COUPLED ATOM CAVITY MODES

To begin, we provide a brief review of the open coupled atoms-cavity system with the goal of both providing a framework for understanding the experimental work and for explicitly enumerating the assumptions made to reduce this system to a classical two-mode system [48–50]. The dynamics of the system under a classical drive and dissipation are then studied with the goal of obtaining the full complex response of the reflected and transmitted cavity field. Finally, a discussion of the probe signal-to-noise sets the stage for addressing measurement resolution at the projection noise level in Sec. III.

A. Linearized response

We consider atoms with two ground states $|\uparrow\rangle$ and $|\downarrow\rangle$ whose populations we wish to estimate [see Fig. 1(b)]. Atoms in $|\uparrow\rangle$ can interact with a cavity mode by absorbing a cavity photon and being promoted to an optically excited state $|e\rangle$. On the other hand, atoms in $|\downarrow\rangle$ are assumed to not interact with the cavity mode because of dipole selection rules, a large energy splitting between the ground states, or otherwise. We note that a coherence can exist between $|\uparrow\rangle$ and $|\downarrow\rangle$, as would be required for sensing a quantum phase, but this coherence is not important for the discussion in this section. In the absence of dissipation, the coupled atoms-cavity system is well described by the Tavis-Cummings Hamiltonian:

$$H = \hbar\delta_c \hat{c}^\dagger \hat{c} + \hbar \sum_{i=1}^{N} g_i \left(\hat{\sigma}_{i-}\hat{c}^\dagger + \hat{\sigma}_{i+}\hat{c}\right) . \qquad (1)$$

The Hamiltonian is written in a frame rotating at the atomic transition $|\uparrow\rangle \to |e\rangle$ angular frequency $\omega_{\uparrow e}$. The parameter g_i sets the coupling strength between the cavity field and the ith atom. There are N atoms total. The operators $\hat{c}^\dagger$ and $\hat{c}$ are the creation and annihilation operators for the cavity field with commutation relations $\left[\hat{c}, \hat{c}^\dagger\right] = 1$ and photon number operator $\hat{M}_c = \hat{c}^\dagger\hat{c}$. The cavity detuning $\delta_c = \omega_c - \omega_{\uparrow e}$ is the difference between the empty cavity frequency ω_c and the atomic transition frequency. Finally, the raising and lowering operators for the ith atom are $\hat{\sigma}_{i+} = |e_i\rangle\langle\uparrow_i|$, and $\hat{\sigma}_{i-} = |\uparrow_i\rangle\langle e_i|$ respectively. The number of atoms in each state is given by the collective projection operators $\hat{N}_\uparrow = \sum_{i=1}^{N} |\uparrow_i\rangle\langle\uparrow_i|$, $\hat{N}_\downarrow = \sum_{i=1}^{N} |\downarrow_i\rangle\langle\downarrow_i|$, and $\hat{N}_e = \sum_{i=1}^{N} |e_i\rangle\langle e_i|$. For brevity, we use the following abbreviations throughout this paper: $N_\uparrow \equiv \left\langle \hat{N}_\uparrow \right\rangle$, $N_\downarrow \equiv \left\langle \hat{N}_\downarrow \right\rangle$ and $N_e \equiv \left\langle \hat{N}_e \right\rangle$.

Although the atoms may in general exist in a superposition of spin up and spin down, in the following analysis we will consider the atoms to be in a definite eigenstate $N_\uparrow$ of the $\hat{N}_\uparrow$ operator. We will then reintroduce the fluctuations in the operator $\hat{N}_\uparrow$ for atoms in a superposition of $|\uparrow\rangle$ and $|\downarrow\rangle$ in terms of the rms projection noise about the mean value $\Delta N_\uparrow = \sqrt{\left\langle (\hat{N}_\uparrow - \langle \hat{N}_\uparrow \rangle)^2 \right\rangle}$.

We assume that the system is driven weakly so that the mean number of atoms in the optically excited state $|e\rangle$ is a small fraction of the total number of atoms in $|\uparrow\rangle$, such that $N_e/N_\uparrow \ll 1$. We also assume that the coupling is uniform $g_i = g$ (with appropriate renormalization of g and N in the case of inhomogeneous coupling provided in Ref. [1]). In the weak excitation limit, one can make the Holstein-Primakoff approximation [51] that essentially replaces the three-dimensional Bloch vector describing the two-level system composed of states $|e\rangle$ and $|\uparrow\rangle$ by its vector projection onto the two dimensional $x-y$ plane [Fig. 3(a)]. When no probe light is applied, the system relaxes into its ground state orientation $-\hat{\mathbf{z}}$. When the system is weakly excited by probe light, and a small fraction of the atoms is promoted to the optically excited state, the lowest order effect on the Bloch vector is a small angular deflection of the Bloch vector away from $-\hat{\mathbf{z}}$.

In this approximation, one replaces the atomic ladder operators with effective creation and annihilation operators as $\sum_i^N \hat{\sigma}_{i+} \approx \sqrt{N_\uparrow}\hat{a}^\dagger \sqrt{1-\frac{\hat{a}^\dagger\hat{a}}{N_\uparrow}}$, and $\sum_i^N \hat{\sigma}_{i-} \approx \sqrt{N_\uparrow}\sqrt{1-\frac{\hat{a}^\dagger\hat{a}}{N_\uparrow}}\,\hat{a}$. In the limit of low atomic saturation $N_e \ll N_\uparrow$, the creation and annhilation operators reduce to $\hat{a}^\dagger \approx \frac{1}{\sqrt{N_\uparrow}}\sum_i^N \hat{\sigma}_{i+}$, and $\hat{a} \approx \frac{1}{\sqrt{N_\uparrow}}\sum_i^N \hat{\sigma}_{i-}$. The number of atoms in $|e\rangle$ is given by the number operator $\hat{N}_e = \hat{a}^\dagger\hat{a}$.

The resulting Hamiltonian describes the coherent coupling of two ring cavities through a beam-splitter whose transmission coefficient increases with the number of atoms in $|\uparrow\rangle$, i.e.,

$$H = \hbar\delta_c \hat{c}^\dagger\hat{c} + \hbar\sqrt{N_\uparrow}g\left(\hat{a}\hat{c}^\dagger + \hat{a}^\dagger\hat{c}\right) . \tag{2}$$

This model is shown in Fig. 3(b). The coupled Heisenberg equations of motion for the cavity and atomic operators are

$$\begin{aligned} \frac{d\langle\hat{c}\rangle}{dt} &= -\imath\delta_c\langle\hat{c}\rangle - \imath\sqrt{N_\uparrow}g\langle\hat{a}\rangle \ , \\ \frac{d\langle\hat{a}\rangle}{dt} &= -\imath\sqrt{N_\uparrow}g\langle\hat{c}\rangle \ . \end{aligned} \tag{3}$$

We can solve for the eigenfrequencies of the coupled equations in terms of the cavity detuning δ_c and the collective vacuum Rabi frequency $\Omega_\uparrow \equiv \sqrt{N_\uparrow}2g$ using

$$\omega_\pm = \frac{\delta_c \pm \sqrt{\delta_c^2 + \Omega_\uparrow^2}}{2} . \tag{4}$$

The collective vacuum Rabi splitting $\Omega_\uparrow$ sets the difference in the normal mode frequencies $\omega_+ - \omega_-$ at zero detuning $\delta_c = 0$. The normal mode frequencies in the laboratory frame are $\omega_{\uparrow e} + \omega_\pm$. A useful relation for simplifying expressions involving the mode frequencies is $\omega_+\omega_- = -\Omega_\uparrow^2/4$.

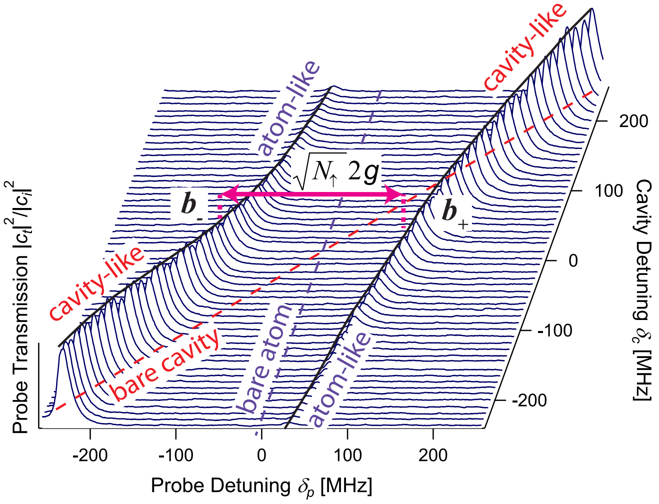

FIG. 4. (Color online) The normal modes of the coupled atoms-cavity system $\mathbf{b}_\pm$ exhibit an avoided crossing in the transmission spectrum at $\delta_c = 0$, where the size of the collective vacuum Rabi splitting is $\Omega_\uparrow = \sqrt{N_\uparrow}2g$.

Any arbitrary superposition of atomic and cavity amplitudes can be written in terms of complex normal mode amplitudes $B_\pm$ and unit vectors $\mathbf{b}_\pm$ as $(\langle\hat{c}\rangle, \langle\hat{a}\rangle) = e^{-\imath\omega_+ t}B_+\mathbf{b}_+ + e^{-\imath\omega_- t}B_-\mathbf{b}_-$. At resonance $\delta_c = 0$, the normal mode vectors are $\mathbf{b}_\pm = (1, \pm 1)/\sqrt{2}$, and the normal modes beat against one another at relative frequency $\Omega_\uparrow$. For example, if at $t = 0$ there are no atoms in the excited state, then $B_\pm = 1/\sqrt{2}$. The light in the cavity will Rabi flop (or be converted) into purely excited-state atoms after a time $\pi/\Omega_\uparrow$, and then Rabi flop back into light in the cavity after $2\pi/\Omega_\uparrow$.

More generally, the unit vectors can be expressed in terms of a mode-mixing angle $\theta_m = \arctan(\omega_-/\omega_+)$ as $\mathbf{b}_+ = (\cos\theta_m, \sin\theta_m)$, and $\mathbf{b}_- = (-\sin\theta_m, \cos\theta_m)$. When $\delta_c \gg \Omega_\uparrow$, the $\mathbf{b}_+$ normal mode is predominantly cavity-like, while the $\mathbf{b}_-$ normal mode is predominantly atom-like. The converse is true when $\delta_c \ll -\Omega_\uparrow$. This normal mode structure is demonstrated in Fig. 4 with an experimental measurment of the transmitted probe power through the cavity as a function of the probe laser frequency and the cavity detuning δ_c.

B. Driven and damped dynamics

The Heisenberg equations of motion of Eq. (3) can be extended to include cavity damping and driving, as well as atomic damping via free space scattering of light (i.e., not into the cavity mode) as follows:

$$\begin{aligned} \frac{d\langle\hat{c}\rangle}{dt} &= -\left(\imath\delta_c + \frac{\kappa}{2}\right)\langle\hat{c}\rangle - \imath\sqrt{N_\uparrow}g\langle\hat{a}\rangle + \sqrt{\kappa_1}c_i \, , \\ \frac{d\langle\hat{a}\rangle}{dt} &= -\frac{\Gamma}{2}\langle\hat{a}\rangle - \imath\sqrt{N_\uparrow}g\langle\hat{c}\rangle \ . \end{aligned} \tag{5}$$

These equations include the additional non-unitary damping and drive terms shown schematically in Fig. 3(b). The additional terms can be derived using input-output theory [52] and will now be discussed. But first, we note that at large $\Omega_\uparrow$, the finite damping terms introduce small corrections to $\omega_\pm$ of order $(\Gamma-\kappa)^2/\Omega_\uparrow$ [53] that may be safely neglected in this paper.

1. Cavity damping and input-output fields

As shown in Fig. 3(b), the damping of the cavity field at rate $\kappa/2=(\kappa_1+\kappa_2+\kappa_L)/2$ is set by the mirror power transmission coefficients $T_{1,2}$ such that $\kappa_{1,2}=T_{1,2}\times f_{\mathrm{FSR}}$. The total round-trip scattering and absorption fractional power losses at the mirrors L can be modelled by an additional beam splitter with field decay rate $\kappa_L=L\times f_{\mathrm{FSR}}$. Here, the cavity free spectral range is $f_{\mathrm{FSR}}=c/2l$, with $2l$ being the round-trip cavity length, and c the speed of light.

The cavity field is driven by an external incident probe field described by the complex amplitude c_i. The reflected and transmitted complex field amplitudes, c_r and c_t respectively, will be detected to infer the number of atoms in $|\uparrow\rangle$. The external field normalizations are chosen such that $|c_{i,r,t}|^2$ is the flux of incident, reflected, and transmitted probe photons in units of photons/second. The average number of incident, reflected, and transmitted photons $M_{i,r,t}$ in a measurement time interval from t' to $t'+T_m$ is then

$$M_{i,r,t}=\int_{t'}^{t'+T_m}|c_{i,r,t}(t'')|^2\,\mathrm{d}t''. \tag{6}$$

It is often convenient to express the number of probe photons coupled into the atoms-cavity system in terms of the measured “missing” photons in the reflected mode compared to the incident beam $M_m\equiv M_i-M_r$.

The reflected and transmitted fields can be found by first solving the coupled-driven Eq. (5) for $\langle\hat{c}\rangle$ and then using the results in the approximate relationships

$$\begin{aligned}c_r&=\sqrt{\kappa_1}\,\langle\hat{c}\rangle-c_i\,,\\ c_t&=\sqrt{\kappa_2}\,\langle\hat{c}\rangle\,,\end{aligned} \tag{7}$$

that hold in the limit of a high finesse cavity $T_{1,2},L\ll 1$.

2. Atomic damping via free space decay

The atomic damping via scattering of light into free space (i.e., not into the cavity mode) is described by an effective amplitude damping rate $\Gamma/2$. To good approximation, the probability decay rate Γ is simply the single-particle excited state $|e\rangle$ decay rate in free space [54]. The rate of scattering into free space is described by the field amplitude $a_s=\sqrt{\Gamma}\,\langle\hat{a}\rangle$, normalized such that the rate of photons scattered into free space is simply $\dot{M}_s=|a_s|^2$.

The above picture of atomic damping can be further refined as shown in Fig. 3(b). While the decay of excitation from the cavity mirrors is single-mode in nature, the atoms scatter light into many free space modes. This multimode scattering can be envisioned by replacing the single decay process via a single mirror with a weak beam splitter for each atom in $|\uparrow\rangle$. If the ensemble is optically thin along all directions except the cavity mode, then one can approximate that each atom decays into its own bath of states with an amplitude $a_{s,i}=\sqrt{\Gamma}\left(\langle\hat{a}\rangle/\sqrt{N_\uparrow}\right)$. The normalization is necessary to impose the fact that if a single photon is emitted into free space, the probability that it was the ith atom that scattered the photon is reduced as the number of atoms $N_\uparrow$ increases. The total scattering rate is the incoherent sum of the decay rates, reproducing the previous decay rate $\dot{M}_s=\Gamma\,|\langle\hat{a}\rangle|^2$. However, this refinement importantly emphasizes that the multimode free space scattering leads to in-principle information gain as to which particular atoms are in $|\uparrow\rangle$, causing single particle collapse of the atomic wavefunction from a coherent superposition into an energy eigenstate, for example $(|\uparrow\rangle+|\downarrow\rangle)/\sqrt{2}\rightarrow|\uparrow\rangle$, thus destroying coherence. In contrast, the decay of light through the cavity mirrors leads to only collective information as to how many atoms total are in spin up and therefore preserves coherence. Thus information gained through the cavity will be useful for preparing conditionally spin-squeezed states, while the free space scattering is a competing decoherence mechanism that serves to reduce the attainable degree of spin squeezing.

3. Dressed mode linewidth

The atomic and cavity damping cause the normal modes to decay, resulting in a mode broadening with approximate Lorentzian full width at half maximum (FWHM) resonance linewidth given by a weighted average linewidth as

$$\kappa'_\pm=\frac{4\omega_\pm^2\kappa+\Omega_\uparrow^2\Gamma}{4\omega_\pm^2+\Omega_\uparrow^2}\,. \tag{8}$$

For atom number counting, we find that the dressed cavity mode that is farthest from atomic resonance is most useful. For brevity, we refer to this mode's linewidth as simply κ' such that $\kappa'=\kappa'_\pm$ when $|\omega_\pm|\geq|\omega_\mp|$.

C. Full complex field response to probing

The reflected and transmitted fields relative to the incident field $c_{r,t}/c_i=I_{r,t}+\imath Q_{r,t}$ can be described in the complex plane by the real amplitudes $I_{r,t}$ and $Q_{r,t}$. We consider a single incident probe frequency close to resonance such that the probe frequency ω_p is detuned from one of the two resonances by $\delta_{p\pm}=(\omega_p-\omega_\pm)$. We assume the probe is near resonance $|\delta_{p\pm}|\ll\omega_+-\omega_-$ such that

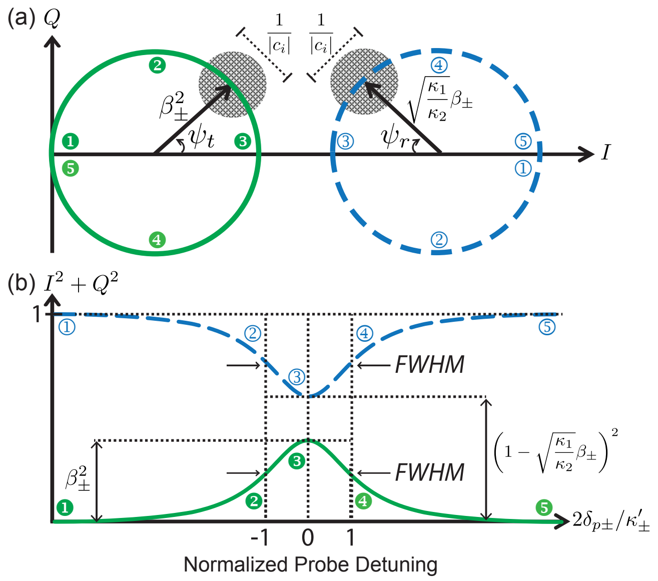
(a) Q
$\frac{1}{|c_i|}$
$\frac{1}{|c_i|}$
$\beta_\pm^2$
ψ_t
$\sqrt{\frac{\kappa_1}{\kappa_2}}\beta_\pm$
ψ_r
I
① ② ③ ④ ⑤
(b) I^2+Q^2
1
FWHM
FWHM
$\left(1-\sqrt{\frac{\kappa_1}{\kappa_2}}\beta_\pm\right)^2$
$\beta_\pm^2$
$2\delta_{p\pm}/\kappa'_\pm$
-1
0
1
Normalized Probe Detuning

FIG. 5. (Color online) Transmitted and reflected probe electric fields from driving the atoms-cavity system through the cavity mode. (a) The electric fields trace out circles in the $I-Q$ phase plane as the probe detuning $\delta_{p\pm}$ from the dressed cavity resonance varies from far-below to far-above resonance. The normalization is chosen such that the reflected electric field goes to 1 when far off resonance. The quantum noise of the probe normalized to the incident electric field is represented as a fuzzy blob with rms diameter $1/|c_i|$. In this illustration, a symmetric cavity $\kappa_1=\kappa_2$ is assumed, so that the circles have the same radius. (b) Corresponding power transmission and reflection.

interference effects between normal modes can be ignored and that the modes are well resolved $\kappa'_\pm \ll \omega_+ - \omega_-$. The normalized transmitted electric field through the cavity is then to good approximation:

$$I_t = \frac{\beta_\pm}{1+\left(2\delta_{p\pm}/\kappa'_\pm\right)^2}\,, \tag{9}$$

$$Q_t = \frac{\beta_\pm\left(2\delta_{p\pm}/\kappa'_\pm\right)}{1+\left(2\delta_{p\pm}/\kappa'_\pm\right)^2}\,. \tag{10}$$

The unitless amplitude $\beta_\pm$ is given by

$$\beta_\pm = \frac{2\sqrt{\kappa_1\kappa_2}}{\kappa+\Gamma\left(\frac{\Omega_\uparrow}{2\omega_\pm}\right)^2}\,. \tag{11}$$

From Eq. (7), the reflected field c_r is just the sum of the transmitted field (rescaled for relative transmission coefficients) and the largely reflected field such that $I_r = 1-\sqrt{\kappa_1/\kappa_2}I_t$, and $Q_r=\sqrt{\kappa_1/\kappa_2}Q_t$.

As shown in Fig. 5(a), the phasor c_t traces out a circle of radius $\beta_\pm/2$ in the complex plane as $\delta_{p\pm}$ varies from $\ll \kappa'_\pm/2$ to $\gg \kappa'_\pm/2$. The translation $I'_t = I_t - \beta_\pm/2$ centers the circle traced out by the phasor $I'_t + \imath Q_t$ at the origin. One then sees that the angle with respect to the real axis is given by $\psi_\pm = \arctan(Q_t/I'_t) = \arctan(2\delta_{p\pm}/\kappa'_\pm)$. A similar translation holds for the reflected field.

D. Probe vacuum noise and measurement resolution

The size of the quantum vacuum noise that contributes uncertainty to measuring the position of the phasor is not changed by a linear transformation of coordinates in the complex plane. For our purposes, the noise can be described as a Gaussian probability distribution with equal and uncorrelated real and imaginary rms fluctuations of magnitude $\sigma_v = 1/2$. The rms quantum vacuum uncertainty $\Delta\psi$ on the angle ψ is then independent of the average value ψ and is set only by the average number of detected photons in transmission $M_d = q_d M_t$as

$$\Delta\psi = \frac{1}{2\sqrt{M_d}}\,. \tag{12}$$

The detection quantum efficiency q_d includes any light loss and any excess technical or thermal noise of the detector relative to vacuum noise. The uncertainty $\Delta\psi$ maps onto an uncertainty on the estimation of $\delta_{p\pm}$ through $\Delta\delta_{p\pm} = |d\delta_{p\pm}/d\psi|\,\Delta\psi = \kappa'_\pm\Delta\psi/2\eta_d$. The detection sensitivity η_d is given by

$$\eta_d = \frac{1}{1+\left(2\delta_{p\pm}/\kappa'_\pm\right)^2}\,. \tag{13}$$

Probing near resonance $\delta_{p\pm}=0$, one finds $\eta_d=1$. For side-of-fringe probing $\delta_{p\pm}=\kappa'_\pm/2$, one finds $\eta_d=1/2$. If the probe frequency is linearly and adiabatically scanned from $\delta_{p\pm}\ll\kappa'_\pm$ to $\delta_{p\pm}\gg\kappa'_\pm$ such that the total number of detected photons is fixed to the same M_d as in the two previous scenarios, one finds $\eta_d=1/2$. The optimal readout assumes that as $\delta_{p\pm}$ is changed, an adaptive homodyne readout is employed to maximize the measurement sensitivity to small changes in ψ. In Ref. [1], heterodyne detection is employed so that adaptive detection is not required. However, the effective quantum efficiency q_d was reduced by 1/2 as a result of the heterodyne detection.

It is straightforward to extend the analysis to a probe signal detected in reflection. However, one must parameterize in terms of the measurable average number of missing photons in the reflection port M_m and the average number of incident photons M_i such that in Eq. (12), one substitutes $M_d \rightarrow (\kappa_2/\kappa_1)M_i q_d(1+\sqrt{1-M_m/M_i})^2$.

III. QUANTUM-LIMITED SIGNAL-TO-NOISE AND FREE SPACE SCATTERING

The measurement of the atomic population $N_\uparrow$ in $|\uparrow\rangle$ is achieved by precisely measuring the dressed mode frequency ω_+ or ω_- or some combination of the two. In essence, the approach used here converts the problem of measuring an atomic population into a frequency measurement. For atoms in a coherent superposition of $|\uparrow\rangle$ and $|\downarrow\rangle$, quantum projection noise in the atomic population $N_\uparrow$ causes the dressed mode frequency to fluctuate. In this section, we first derive the fluctuations on

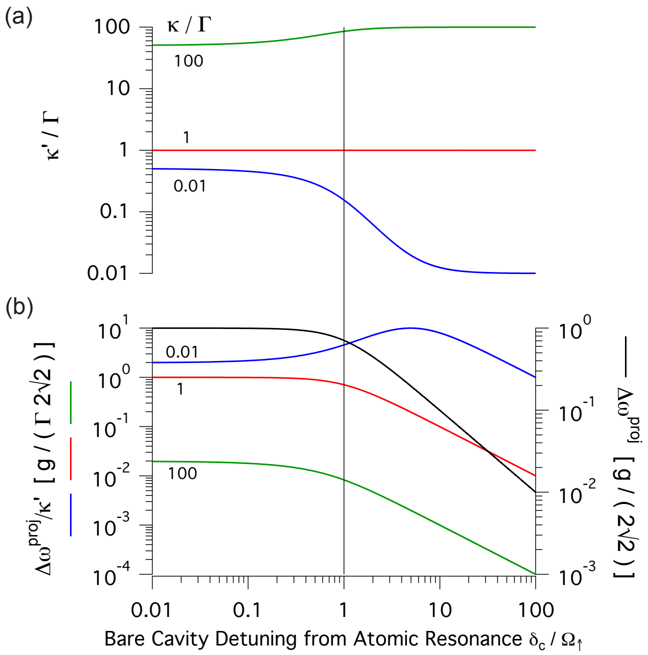

FIG. 6. (Color online) Theoretical scaling of key quantities with cavity detuning δ_c expressed in units of the the collective vacuum Rabi frequency $\Omega_\uparrow$. (a) The dressed cavity linewidth κ' in units of the atomic excited state linewidth Γ. In (a) and (b), the scaling for different cavity finesses is shown for $\kappa/\Gamma = 0.01$, 1, and 100 (blue, red, and green, respectively). (b, right, black curve) The rms fluctuation of the dressed cavity mode frequency due to projection noise fluctuations $\Delta\omega_+^{\rm proj}$ decreases as $1/\delta_c$ above $\delta_c/\Omega_\uparrow = 1$. The normalization is chosen such that one should multiply by $g/2\sqrt{2}$. (b, left, red, blue, green curves). The ratio of the projection noise fluctuation of the cavity mode to the dressed cavity linewidth $\Delta\omega^{\rm proj}/\kappa'$ is shown normalized such that the plotted values should be multiplied by $g/(2\sqrt{2}\Gamma)$. A large ratio is desirable because technical noise may limit the ability to split the probed resonance by more than a fractional amount.

the dressed mode frequency due to quantum projection noise as a function of cavity detuning δ_c. We then use the results of Sec. II to obtain the average number of free-space-scattered photons per atom $m_s^{\rm proj}$, when the measurement resolution on the probe field is sufficient to resolve the projection noise fluctuations of the mode frequency $\Delta\omega^{\rm proj}$. The quantity $m_s^{\rm proj}$ is the key figure of merit that characterizes the degree to which a measurement is non-demolition. Three limits of cavity probing are identified, and a summary table of various key quantities in different regimes is presented.

A. Projection-noise-driven fluctuations of mode frequencies

As stated earlier, the atom number $N_\uparrow$ can be determined by precisely measuring the dressed mode frequency ω_+ or ω_- with a cavity probe. The collective enhancement of the Rabi splitting by $\sqrt{N_\uparrow}$ produces a key enhancement of the measurement sensitivity needed to resolve projection noise. To concretely analyze the signal to noise of the probing, we consider a measurement procedure most relevant to spectroscopy: we assume that for each experimental trial, all of the $N \gg 1$ total atoms are initially prepared in spin down via optical pumping or otherwise. Each atom is then rotated into an equal superposition of spin up and down, preparing the ensemble

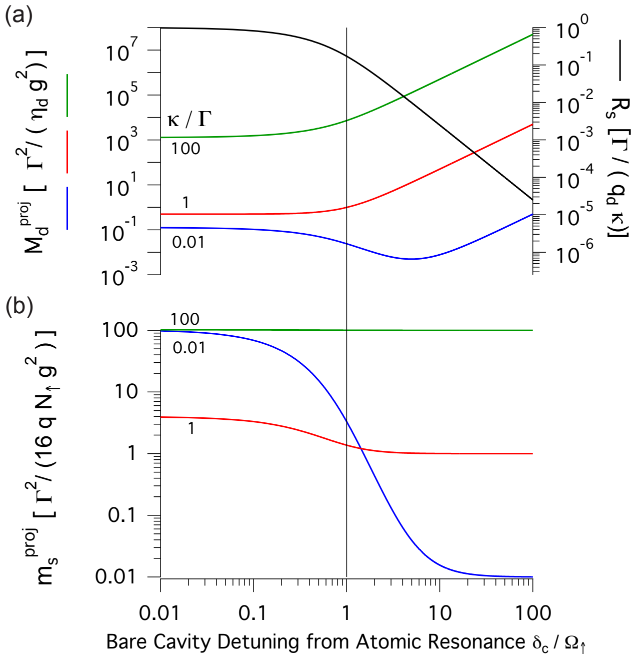

FIG. 7. (Color online) Theoretical scaling of key quantities with cavity detuning δ_c expressed in units of the the collective vacuum Rabi frequency $\Omega_\uparrow$. In (a) and (b), the scaling for different cavity finesses is shown giving $\kappa/\Gamma = 0.01$, 1, and 100 (blue, red, and green, respectively). (a, left, blue, red, green) The average number of detected photons needed to resolve the projection noise fluctuations $M_d^{\rm proj}$ normalized such that the plotted values should be multiplied by $\Gamma^2/(\eta_d g^2)$. (a, right, black) The ratio of the number of free-space-scattered photons for every detected photon R_s, normalized such that the plotted values should be multiplied by $\Gamma/(q_d\kappa)$. (b) The crucial average number of scattered photons into free space per atom $m_s^{\rm proj}$ when the atomic population measurement precision is equal to the projection noise fluctuations. The normalization is such that the plotted values should be multiplied by $\Gamma^2/(16 q N_\uparrow g^2)$. In the bad-cavity limit of $\kappa \gg \Gamma$ (green curves), there is little fundamental advantage to operating away from resonance $\delta_c = 0$. The technical requirements are simply increased as a result of detuning. As the finesse of the cavity F is increased, the amount of free space scattering falls roughly as $1/F$ until the good cavity regime is reached when $\kappa \ll \Gamma$ (blue curves). Here, one must detune by roughly the critical detuning δ_c° in order to realize the full advantage of having increased the cavity finesse. Importantly, note that $m_s^{\rm proj}$ does not significantly decrease above δ_c° owing to cancellation in this regime of the scaling of $R_s \sim 1/\delta_c^2$ with the scaling of $M_d^{\rm proj} \sim \delta_c^2$.

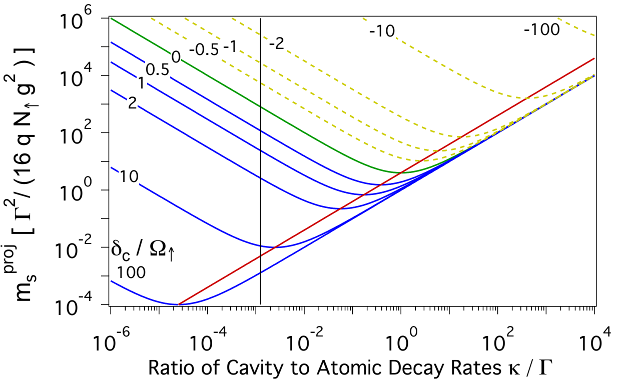

FIG. 8. (Color online) The crucial average number of scattered photons into free space per atom such that the detected probe light allows resolution of projection noise fluctuations m_s^{proj} versus the ratio of the cavity power to atomic population decay rates κ/Γ. The normalization is chosen such that the plotted values should be multiplied by $\Gamma^2/(16qN_\uparrow g^2)$. Here, we assume that κ is varied by changing the cavity finesse while holding the cavity length fixed (such that g is constant). Each trace represents a fixed ratio of the bare cavity detuning to the collective vacuum Rabi frequency $\delta_c/\Omega_\uparrow$, with values labeled on the traces and blue denoting $\delta_c/\Omega_\uparrow > 0$, green $\delta_c/\Omega_\uparrow = 0$ and dashed yellow $\delta_c/\Omega_\uparrow < 0$. Here we consider probing the dressed mode at frequency ω_+. At a fixed detuning (and therefore fixed projection-noise-driven frequency fluctuation size) a minimum is reached below which a better cavity is detrimental due to the dressed cavity linewidth κ' becoming clamped while the ratio of free space scattering to detected photon number R_s continues to rise. In the units above, the locus of the minimum is just $4\kappa/\Gamma$ (red line). Including the normalization, the locus of the minimum reduces to $m_s^{\mathrm{proj}} = 1/(qN_\uparrow C)$. When including the dependence of g^2, $\kappa \sim 1/l$ on cavity length l, the minimum value of m_s^{proj} is not changed by just shortening the cavity at fixed finesse. Only shortening the cavity length while simultaneously increasing the cavity finesse (such that κ is constant) leads to a net fundamental reduction of m_s^{proj}. Finally, the vertical black line indicates the cavity linewidth for a finesse $F = 10^6$ cavity, near the highest currently achievable, for ^{87}Rb and $l = 2$ cm.

in a coherent spin state (CSS). The population in spin up and down fluctuate about the average $N_\uparrow = N_\downarrow = N/2$ with equal magnitude but perfectly anti-correlated projection noise fluctuations $\Delta N_\uparrow = -\Delta N_\downarrow = \sqrt{N}/2$.

The rms fluctuation $\Delta\omega^{\mathrm{proj}}$ of the individual mode frequencies $\omega_\pm$ caused by the projection-noise-driven fluctuations in $N_\uparrow$ is found by linear expansion as $\Delta\omega^{\mathrm{proj}} = (d\omega_\pm/dN_\uparrow)\,|_{N_\uparrow}\Delta N_\uparrow$. Evaluating using Eq. (4), one finds

$$\Delta\omega^{\mathrm{proj}} = \frac{g}{2\sqrt{2}} \frac{\sqrt{N_\uparrow}2g}{\sqrt{\left(\sqrt{N_\uparrow}2g\right)^2 + \delta_c^2}} \,. \tag{14}$$

The fluctuations of the two mode frequencies are equal in magnitude but opposite in sign such that the rms differential fluctuation is $\Delta(\omega_+ - \omega_-)^{\mathrm{proj}} = 2\Delta\omega^{\mathrm{proj}}$.

The projection noise variance $(\Delta\omega^{\mathrm{proj}})^2$ decreases as a Lorentzian versus the bare cavity detuning δ_c with half width at half maximum (HWHM) $\sqrt{N_\uparrow}2g$. Figure 6(b) shows this scaling with detuning (black, left curve). The technical requirements on the experiment for resolving $\Delta\omega^{\mathrm{proj}}$ are increased with detuning. Other experimental imprecision and inaccuracies scale relative to the mode linewidth κ' that one must split to the level of $\Delta\omega^{\mathrm{proj}}$, therefore the ratio $\Delta\omega^{\mathrm{proj}}/\kappa'$ is shown in Fig. 6(b, left) for three different bare cavity linewidths $\kappa/\Gamma = 0.01, 1, 100$ (blue, red, green). Note that in the good cavity limit $\kappa/\Gamma \ll 1$ (blue), the experimental requirement on splitting the mode line can be somewhat reduced at larger detuning owing to the rapid fall off of κ' as $1/\delta_c^2$ in the approximate region $\delta_c/\Omega_\uparrow \in \{1, 10\}$.

B. Fundamental measurement noise and free space scattering at arbitrary detuning δ_c

The resonance frequency ω of the farther detuned of the two dressed modes ω_+ or ω_- is measured relative to the known frequency of a coherent (and unsqueezed) laser probe. The rms uncertainty on the probe detuning $\Delta\delta_p$ is equal to the projection noise fluctuation level $\Delta\omega^{\mathrm{proj}}$ at an average detected photon number of

$$M_d^{\mathrm{proj}} = \frac{1}{2\eta_d}\left(\frac{\kappa'}{g}\right)^2\left(1 + \frac{\delta_c^2}{\Omega_\uparrow^2}\right) \,. \tag{15}$$

The passage of light through the cavity also leads to the scattering of $M_s = |a_s|^2 T_m$ probe photons into free space modes by the atoms in spin up. The ratio of free space scattered to detected photons $R_s = M_s/M_d$ is given by a weighted ratio of the two damping rates as

$$R_s = \frac{1}{q_d\eta_s}\frac{\Gamma}{\kappa}\frac{\Omega_\uparrow^2}{4\omega^2} \,. \tag{16}$$

The factor η_s plays an equivalent role to a quantum efficiency and separately accounts for photons exiting the cavity via an undetected port. In the example we consider here, only the transmission port 2 is measured, and $\eta_s = \kappa_2/\kappa$ [see Fig. 3(b)].

From Eqs. (16) and (15), one finds that the number of scattered photons into free space normalized to the total number of atoms N is

$$m_s^{\mathrm{proj}} = \frac{R_s M_d^{\mathrm{proj}}}{N} \tag{17}$$

$$= \frac{1}{4qN_\uparrow C}\left(\frac{\kappa'}{\kappa}\right)^2\left(1 + \frac{\delta_c^2}{\Omega_\uparrow^2}\right)\frac{\Omega_\uparrow^2}{\omega^2} \,. \tag{18}$$

The single particle cooperativity parameter is $C = (2g)^2/\kappa\Gamma$ and the total effective quantum efficiency is

$$q = q_d\eta_d\eta_s \,. \tag{19}$$

For any arbitrary measurement resolution $\Delta\delta_p = \alpha\Delta\omega^{\mathrm{proj}}$ relative to the projection noise level, the required average number of detected photons is simply

$M_d = M_d^{\rm proj}/\alpha^2$, and the average number of scattered photons normalized to the total atom number N is $m_s = m_s^{\rm proj}/\alpha^2$.

A key result is that the free space scattering at a constant measurement precision α saturates to a finite value $m_s^{\rm proj} \rightarrow 1/(4qN_\uparrow C\alpha^2)$ as $|\delta_c| \rightarrow \infty$. This saturation is because in Eq. (18), the ratio of free space to detected photons asymptotically decreases as $1/\delta_c^2$, but the required number of detected photons increases asymptotically as δ_c^2. The non-demolition character of the measurement is ultimately set by the collective cooperativity parameter and quantum efficiency $qN_\uparrow C$. This quantity physically sets the maximum rate at which collective information can be extracted from the ensemble compared to the rate at which single-particle information is gained by the environment via multimode scattering of light into the many modes of free space.

In the good cavity limit $\kappa \ll \Gamma$, the frequency dependence δ_c of Eq. (18) can be understood in three regimes: the far-detuned dispersive regime $|\delta_c| > \delta_c^\circ$, the near-detuned dispersive regime $|\delta_c| < \delta_c^\circ$, and the resonant regime $\delta_c = 0$. The critical cavity detuning δ_c° is given by

$$\delta_c^\circ = \sqrt{\frac{\Gamma}{\kappa}\frac{\Omega_\uparrow}{2}\frac{1}{\sqrt{q}}} = \frac{\Gamma}{2}\sqrt{\frac{N_\uparrow C}{q}}\,. \tag{20}$$

The critical detuning is the cavity detuning at which the dressed cavity linewidth is $\kappa' = 2\kappa$, possible only in the good cavity limit $\kappa \ll \Gamma$. Expressions for the number of photons scattered into free space per atom $m_s^{\rm proj}$, the absolute size of the projection noise fluctuations of the mode frequency $\Delta\omega^{\rm proj}$, and the dressed cavity linewidth κ' are summarized in these different regimes in Table I. Again, the quantity $m_s^{\rm proj}$ is critical for understanding the fundamental limits on both probe-induced heating of the sample and potential improvements on measurement sensitivity beyond the SQL.

C. Minimizing $m_s^{\rm proj}$ at fixed maximum detuning

In some experimental situations, a maximum probe detuning $|\delta_c| \leq \delta_{\rm max}$ is set by the energy structure of the atom. For instance, the ground state hyperfine splitting in ^{87}Rb imposes $\delta_{\rm max} \approx 6.8/2$ GHz [7]. An optimum value of $N_\uparrow C$ can be found that minimizes $m_s^{\rm proj}$ when $|\delta_c| = \delta_{\rm max}$. The scaling for this case is shown in the last line of Table I. Physically, the optimum value of $N_\uparrow C$ is reached (at a fixed detuning) when the dressed cavity linewidth is related to the bare cavity and atomic linewidths by $\kappa'/\kappa = 2\Gamma/(\Gamma+\kappa)$. In the resonant limit, $\delta_c = 0$, one finds an optimum $\kappa'/\kappa = 1$, while in the detuned limit one finds $\kappa' \approx 2\kappa$, i.e., the detuned cavity resonance is broadened by a factor of 2 at optimum. In this same limit, the ratio of rms fluctuation size to dressed cavity HWHM is given by $\Delta\omega^{\rm proj}/(\kappa'/2) = \sqrt{C}/2\sqrt{2}$.

IV. EXPERIMENTAL PROBING IN THE RESONANT LIMIT, $\delta_c = 0$

Here we consider the special case of probing in the resonant limit, $\delta_c = 0$, used in the experiment of Ref. [1]. In Sec. IV A, we give a brief review of the experimental setup. In Sec. IV B, we consider the theoretical results of Sec. III in the limit of $\delta_c = 0$. Sec. IV C and IV D detail technical advantages and sources of common-mode noise rejection obtained by working in the resonant limit and simultaneously probing both dressed cavity modes. Sec. IV E considers the effects of spatial mode mismatch of the probe modes in a standing-wave cavity on the correlation between the dressed mode frequencies. Finally, in Sec. IV F, we provide detailed descriptions of two schemes for probing the dressed mode frequencies at low probe powers.

A. Review of experimental setup

The two-level system whose populations we wish to measure are the clock states $|\uparrow\rangle = |F=2, m_F=0\rangle$ and $|\downarrow\rangle = |F=1, m_F=0\rangle$ of the ^{87}Rb ground electronic state $5^2S_{1/2}$ with microwave transition frequency $\omega_{\rm hf}/2\pi = 6.834$ GHz [see Fig. 1(b)]. An ensemble of approximately 10^6 ^{87}Rb atoms are loaded into the TEM$_{00}$ mode of an optical cavity whose frequency is made resonant with the $|\uparrow\rangle$ to $|e\rangle$ optical transition with wavelength $\lambda = 795$ nm. Here, the electronic excited state is $|e\rangle = |5^2P_{1/2}, F'=1, m_F=0\rangle$. For π-polarized probe light, the states $|\uparrow\rangle$ and $|e\rangle$ form a nearly ideal two-level cavity-QED system because the matrix element between $|\uparrow\rangle$ and the only other nearby state $|5^2P_{1/2}, F=2, m_F=0\rangle$ is zero. Confinement and a fixed spatial registration of the atoms with respect to the cavity mode is accomplished via a 360 μK deep intracavity 1-D optical lattice with wavelength $\lambda_{lat} = 823$ nm. The radial temperature of the atoms is measured to be about 25 μK. The rms extent of the atomic motion in the lattice is $x_{\rm rms} = y_{\rm rms} \approx 10$ μm in the radial directions. In the axial direction, the atoms are trapped in the Lamb-Dicke regime with $z_{\rm rms} \approx 24$ nm and Lamb-Dicke parameter ≈ 0.2.

The spatially averaged cavity cooperativity parameter is $C = 3.2 \times 10^{-3}$, the cavity power decay rate is $\kappa = 2\pi(9.2$ MHz$)$, and the excited state $|e\rangle$ population decay rate is $\Gamma = 2\pi(5.75$ MHz$)$. Over time, we found that the cavity linewidth has increased from 9.2 MHz during the heterodyne Pound-Drever-Hall detection scheme described in Sec. IV F 1 to 11.1 MHz during the heterodyne IQ detection scheme described in Sec. IV F 2. The peak on-axis value of the coupling constant is $2g_\circ = \sqrt{\frac{2cd_{ea}^2}{\hbar\lambda\epsilon_\circ V_m}} = 2\pi(0.607$ MHz$)$. The atomic dipole moment is $d_{ea} = 1.465$ C·m, c is the speed of light, $\epsilon_\circ$ is the electric permittivity of vacuum, and $\hbar$ is Planck's constant. The effective mode volume for our symmetric standing-wave cavity is $V_m = \frac{1}{4}\pi w_0^2 l =$

TABLE I. Regimes of cavity probing. The regime name and assumptions used to define the regime are provided in the first and last columns. The quantity m_s^{proj} is the average number of photons scattered into free space normalized to the total atom number N, required to resolve an rms fluctuation $\sqrt{N_\uparrow/2}$ in the spin up population equal to the projection noise level. The quantity $\Delta\omega^{\mathrm{proj}}$ is the rms angular frequency fluctuation of a single coupled atoms-cavity mode $\omega_\pm$ due to projection noise. The quantity κ' is the dressed cavity power decay linewidth, here taken for the mode detuned farthest from atomic resonance. The single-particle cooperativity C, the number of atoms in spin up $N_\uparrow = N/2$, the single-particle cavity coupling g, the empty cavity power and atomic population decay rates κ and Γ respectively, and the collective vacuum Rabi frequency $\Omega_\uparrow$ are related by the following: $\Omega_\uparrow = \sqrt{N_\uparrow}2g$, $N_\uparrow C = N_\uparrow(2g)^2/\kappa\Gamma$. The detuning of the empty cavity resonance frequency from the atomic transition frequency is δ_c, and the critical detuning at which $\kappa' = 2\kappa$ is $(\delta_c^\circ)^2 = \Omega_\uparrow^2\Gamma/4\kappa$, assuming the good cavity limit $\Gamma \gg \kappa$. The maximally detuned regime assumes that the quantity $N_\uparrow C$ is chosen to minimize m_s^{proj} in the presence of the constraint that the cavity detuning cannot be made larger than some maximum value δ_{max} set by technical constraints on resolving the projection noise fluctuations or fundamental constraints set by the internal energy level structure of the atoms being probed (for instance the ground state hyperfine splitting in ^{87}Rb).

Regime Name	m_s^{proj} $\left[\times\frac{1}{4q}\right]$	$\Delta\omega_\pm^{\mathrm{proj}}$	κ' $[\times\kappa]$	Assumptions
Resonant	$\frac{1}{N_\uparrow C}\left(1+\frac{\Gamma}{\kappa}\right)^2$	$\frac{g}{2\sqrt{2}}$	$\frac{1}{2}\left(1+\frac{\Gamma}{\kappa}\right)$	$\delta_c = 0$
Detuned	$\frac{1}{N_\uparrow C}\left(\frac{\kappa'}{\kappa}\right)^2$	$\sqrt{\frac{N_\uparrow}{2}}\frac{g^2}{\lvert\delta_c\rvert}$	$1+\frac{N_\uparrow g^2}{\delta_c^2}\left(\frac{\Gamma}{\kappa}-1\right)$	$\delta_c \gg \Omega_\uparrow$
Near Detuned, Good Cavity	$N_\uparrow C\frac{\Gamma^4}{(2\delta_c)^4}$	$\sqrt{\frac{N_\uparrow}{2}}\frac{g^2}{\lvert\delta_c\rvert}$	$\frac{N_\uparrow g^2}{\delta_c^2}\frac{\Gamma}{\kappa}$	$\delta_c^\circ \gg \delta_c \gg \Omega_\uparrow; \Gamma \gg \kappa$
Critically Detuned, Good Cavity	$\frac{4}{N_\uparrow C}$	$\frac{g}{\sqrt{2}}\sqrt{\frac{\kappa}{\Gamma}}$	2	$\delta_c = \delta_c^\circ \gg \Omega_\uparrow; \Gamma \gg \kappa$
Far Detuned	$\frac{1}{N_\uparrow C}$	$\sqrt{\frac{N_\uparrow}{2}}\frac{g^2}{\lvert\delta_c\rvert}$	$1+\frac{N_\uparrow g^2}{\delta_c^2}\frac{\Gamma}{\kappa}$	$\delta_c \gg \delta_c^\circ, \Omega_\uparrow; \Gamma \gg \kappa$
Maximally Detuned, Good Cavity, Optimized	$\left(\frac{\Gamma}{2\delta_{\mathrm{max}}}\right)^2$	$\frac{g}{\sqrt{2}}\sqrt{\frac{\kappa}{\Gamma}}$	2	$\delta_c = \delta_{\mathrm{max}} \gg \Omega_\uparrow; \Gamma \gg \kappa;$ $N_\uparrow C = \left(\frac{2\delta_{\mathrm{max}}}{\Gamma}\right)^2$

0.0748 mm^3. The mirror separation is $l = 1.91$ cm, the mode waist $w_0 = 70.6$ μm, and the mode Rayleigh range is $z_R = 1.97$ cm. The axially averaged coupling constant is $2g = 2\pi(0.526$ MHz). Because of the tight confinement of the atoms compared to the waist of the probe mode and the periodicity of the standing-wave probe mode, thermal averaging only slightly reduces $2g$ by 4%.

B. Fundamental scalings related to projection noise

On resonance $\delta_c = 0$, the absolute size of the projection noise fluctuations is maximized, i.e.,

$$\Delta\omega_\pm^{\mathrm{proj}} = \frac{g}{2\sqrt{2}}\,. \tag{21}$$

Note that the rms fluctuation is independent of N, as experimentally demonstrated in Fig. 9. The same is true for the FWHM linewidth which is simply equal to the average linewidth [53] due to the equal photonic and atomic contributions to the normal modes:

$$\kappa'_\pm = (\kappa+\Gamma)/2\,. \tag{22}$$

To be able to resolve projection noise, one must detect, on average, a number of probe photons in transmission given by

$$M_{d\pm}^{\mathrm{proj}} = \frac{1}{2\eta_d}\left(\frac{\kappa'_\pm}{g}\right)^2\,. \tag{23}$$

The ratio of free-space-scattered photons to detected probe photons in transmission is

$$R_{s\pm} = \frac{1}{q_d\eta_s}\frac{\Gamma}{\kappa}\,. \tag{24}$$

Finally, the number of scattered photons into free space for measurement uncertainty at the projection noise level normalized to the total number of atoms N is

$$m_{s\pm}^{\mathrm{proj}} = \frac{1}{2qNC}\left(1+\frac{\Gamma}{\kappa}\right)^2\,. \tag{25}$$

If the cavity length and mode volume are fixed by experimental constraints, then one is, in principle, free to minimize Eq. (25) by varying the finesse of the cavity mirrors, until a minimum value of $m_s^{\mathrm{proj}} = 2/qNC$ is reached when $\kappa = \Gamma$. The minimization with respect to cavity finesse accounts for the fact that the cooperativity C scales as $1/\kappa$.

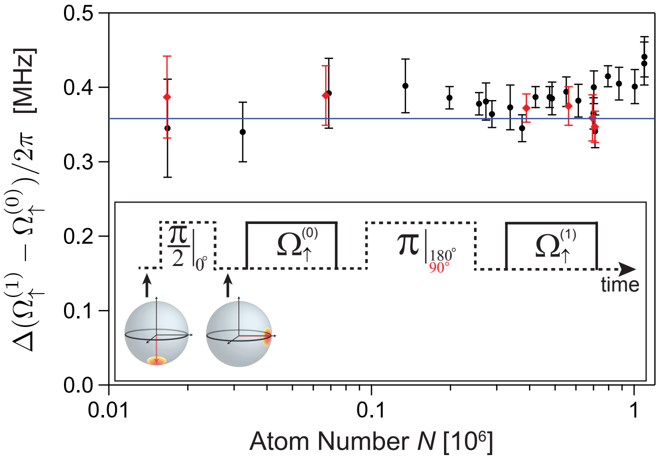

FIG. 9. (Color online) In the resonant limit $\delta_c = 0$, the rms projection noise fluctuation of the population $N_\uparrow$ is independent of total atom number N. Shown here are the measured rms fluctuations of the dressed cavity modes $\Delta(\Omega_\uparrow^{(1)} - \Omega_\uparrow^{(0)})/2\pi$ after subtracting out the probe measurement noise in quadrature. The data agrees with the *a priori* prediction (line) for the projection noise level $\sqrt{2}g/2\pi = 0.358$ MHz very well. At larger atom numbers $N > 7 \times 10^5$, additional technical noise was observed. In contrast, probing in the off-resonant regime results in a cavity mode frequency noise variance that scales linearly with N, and is always smaller than in the resonant limit [see Eq. (14)]. To explore potential added noise from the π-pulse rotation that swaps the two atomic populations $N_\uparrow$ and $N_\downarrow$ between the two splitting measurements, we apply the rotation about an axis perpendicular to the Bloch vector (black points), and about an axis parallel to the Bloch vector (red diamonds).

C. Noise rejection in the resonant limit

Section IV B has outlined fundamental quantum limits on detection in the $\delta_c = 0$ regime. In this subsection, we describe how the $\delta_c = 0$ regime is useful for rejecting other sources of technical noise. Simultaneous probing of both transmission resonances $\omega_\pm$ is advantageous for canceling technical, but important, laser frequency noise and cavity frequency noise. Importantly, the previous analysis for the value of m_s^{proj} is not modified if $M_d^{\mathrm{proj}}/2$ photons are used to measure each mode frequency ω_+ and ω_-.

From Eq. (4), we find that the measured differential quantity $\omega_+ - \omega_- \approx \Omega_\uparrow\left(1 + \frac{\delta_c^2}{2\Omega_\uparrow^2}\right)$ is only quadratically sensitive to the cavity detuning δ_c. Note that the absolute sensitivity to δ_c is decreasing as $1/\sqrt{N_\uparrow}$, a favorable scaling for working with large atom number. As an example, a typical $\Omega_\uparrow/2\pi = 300$ MHz and a detuning of $\delta_c/2\pi = 1$ MHz causes a change in the measured splitting 100 times smaller than projection noise fluctuation in the collective Rabi frequency $\Delta\Omega_\uparrow^{\mathrm{proj}}$.

Simultaneous or near-simultaneous measurements of both resonances can strongly suppress the impact of laser frequency noise. To make these measurements, one can use low phase noise RF modulation of a single laser with much higher phase noise to generate probe components near ω_+ and ω_-. The laser carrier frequency noise is common-mode to the two probes and cancels in the difference $\omega_+ - \omega_-$. The measured power spectral density (PSD) of the probe-cavity relative frequency noise $S_\nu(f)$, shown in Fig. 10, was measured for our system using side-of-fringe transmission. If both the upper and lower transmission resonances are measured for time T_m with time separation τ_m between the measurements, the noise variance in the measured splitting due to laser noise is

$$\left(\frac{\Delta\Omega_\uparrow^{\mathrm{laser}}}{2\pi}\right)^2 = \int_0^\infty S_\nu(f) T(f) \mathrm{d}f\,, \tag{26}$$

where the transfer function $T(f)$ is

$$T(f) = \frac{4\sin^2(\pi f \tau_m)\sin^2(\pi f T_m)}{(\pi f T_m)^2}\,. \tag{27}$$

If the laser possesses a Lorentzian lineshape with FWHM $\Delta\nu$ in Hz as measured in heterodyne versus a perfect reference laser, the PSD is constant with value $S_\nu(f) = \Delta\nu/\pi$. Integrating Eq. (26), we find $(\Delta\Omega_\uparrow^{\mathrm{laser}}/2\pi)^2 = S_\nu\tau_m/T_m^2$ for good time overlap $\tau_m < T_m$, and S_ν/T_m for no time overlap $\tau_m > T_m$. Completely unoverlapped measurements would yield an absolute measurement uncertainty of $\Delta\Omega_\uparrow^{\mathrm{laser}}/2\pi = \sqrt{\Delta\nu B_m/\pi}$, the geometric mean of the measurement bandwidth $B_m = 1/T_m$ and the laser FWHM linewidth $\Delta\nu$. For a typical extended-cavity-diode-laser $\Delta\nu = 100$ kHz, and $\Delta\Omega_\uparrow^{\mathrm{laser}}/2\pi \approx 180\ \mathrm{kHz}\sqrt{\mu\mathrm{s}/T_m}$. For partial time overlap $\Delta\Omega_\uparrow^{\mathrm{laser}}/2\pi \approx 180\ \mathrm{kHz}\sqrt{\mu\mathrm{s}}\sqrt{\tau_m/T_m^2}$.

In practice, lasers exhibit low frequency $1/f$ noise, but so long as $1/\tau_m$ is much larger than the noise corner frequency, the above description is adequate. The laser noise can be reduced by spreading the M_d detected probe photons over a longer measurement period, but at the possible expense of additional decoherence of the atomic quantum state and the potential additional contributions from $1/f$ laser and cavity frequency noise.

D. ac Stark shift cancellation

The intracavity probe light induces an ac Stark or light shift of the $|\uparrow\rangle$ state. At resonance, simultaneous probing of both modes $\omega_\pm$ leads to a cancellation of the shift as the induced shifts have opposite signs as the two modes are symmetrically spaced above and below the atomic transition frequency $\omega_{\uparrow e}$. In the case of inhomogeneous coupling of the atoms to the cavity mode (as was the case in Ref. [1]), the ac Stark shifts are inhomogeneous and lead to a loss of signal and a reduction in the effectiveness of composite pulse sequences used for manipulating the ground state spin manifold. The integrated phase

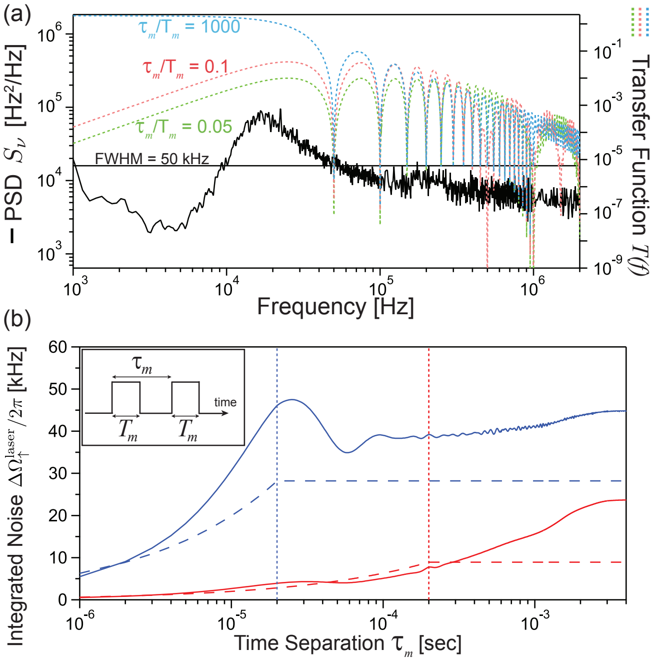

FIG. 10. (Color online) (a) Measured probe laser frequency noise spectrum $S_\nu(f)$ (solid black curve) and for reference the calculated white frequency noise level for a Lorentzian 50 kHz FWHM linewidth laser (horizontal black line). Also shown are theoretical transfer functions relating laser frequency noise to Rabi splitting noise for $T_m = 20\mu$s and $\tau_m/T_m = 0.05, 0.1, 1000$ (dotted green, blue, and red curves, respectively) The inset of (b) defines the measurement timeing. For the case $\tau_m/T_m = 1000$, the $\sin^2(\pi f T_m)/(\pi f T_m)^2$ envelope of the transfer function is shown here. obtained by averaging over the underlying fast oscillations. (b) RMS noise in the Rabi splitting noise $\Delta\Omega_\uparrow^{\text{laser}}/2\pi$ due to the measured laser frequency noise versus τ_m for $T_m = 20$ μs (solid blue curve) and for $T_m = 200$ μs (solid red curve). For a white laser frequency noise spectrum of the level shown in (a), the integrated Rabi splitting noise spectrum versus τ_m is shown in dashed blue and red curves. Vertical dashed lines indicate the two different T_m used for the transfer function integration. Most of the integrated noise at larger τ_m can be attributed to the laser frequency noise bump near 17 kHz.

shift caused by passing probe light through the cavity was measured using a microwave Ramsey sequence and observing the phase shift of the Ramsey fringe versus the number of photons coupled into the atoms-cavity system. In Fig. 11, we show the probe-induced phase shift if only the ω_+ mode or the ω_- mode is probed. We then show the high degree of cancellation of the phase shift, and therefore the average induced ac Stark shift, when both the ω_+ and ω_- modes are probed simultaneously.

E. Spatial mode matching of atoms-cavity modes

In a standing-wave cavity, the $\omega_\pm$ modes arise due to coupling of the cavity mode to atoms located away from the nodes of the standing-wave of each mode. By probing at two different frequencies, it is possible that the two standing-wave probe modes effectively couple to two slightly different sub-ensembles of atoms. Projection noise fluctuations in the two sub-ensembles are not perfectly correlated such that the fluctuations of ω_+ and ω_- are also no longer perfectly correlated. The contribution of projection noise to the difference of the mode frequencies $\omega_+ - \omega_-$ would then be reduced. In the extreme limit of the nodes of the ω_+ mode being aligned with the antinodes of the ω_- mode, the two sub-ensembles are completely independent, the projection noise driven rms fluctuations of the difference $\Delta(\omega_+ - \omega_-)$ would be $\sqrt{2}$ lower than for the case of perfect overlap. Here we calculate this effect and provide numerical results indicating that this effect is small in the experiment of Ref. [1].

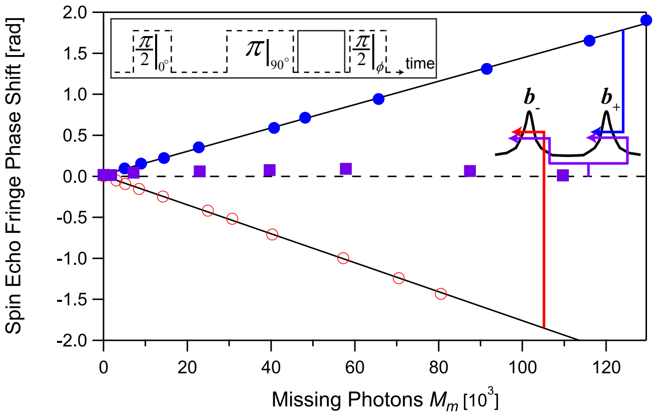

FIG. 11. (Color online) The relative quantum phase between states $|\uparrow\rangle$ and $|\downarrow\rangle$ is light shifted by passing probe photons through the atoms-cavity system near only the upper normal mode frequency ω_+ (blue solid circles) or only near the lower normal mode frequency ω_- (red open circles). The shifts have opposite sign and cancel if probe photons are simultaneously passed through the atoms-cavity system at both frequencies (purple squares). The measurements are performed using a variable number of photons coupled into the atoms-cavity system M_m during a microwave spin-echo sequence (inset) employed to remove background dephasing from the trapping optical lattice.

In vacuum, the wave vectors for resonant probe light $k_\pm = \omega_\pm/c$ have a differential wave vector given by $k_+ - k_- = \Omega_\uparrow/c$. However, if the atoms uniformly fill the cavity mode along the axial or $\hat{z}$ direction, then the index of refraction of the atoms at the resonant frequencies $\omega_\pm$ must be such that two wavevectors $k'_\pm = n_\pm k_\pm$ are identical inside the atomic medium. This is guaranteed by the round trip phase being a multiple integer of 2π at resonance.

If, however, the atoms do not uniformly fill the cavity, then the wavevectors of the probe modes in vacuum and inside the atomic ensemble can be different, leading to coupling to slightly different atomic sub-ensembles. Using the original condition, one finds the indices of refraction of the atomic ensemble at position z along the

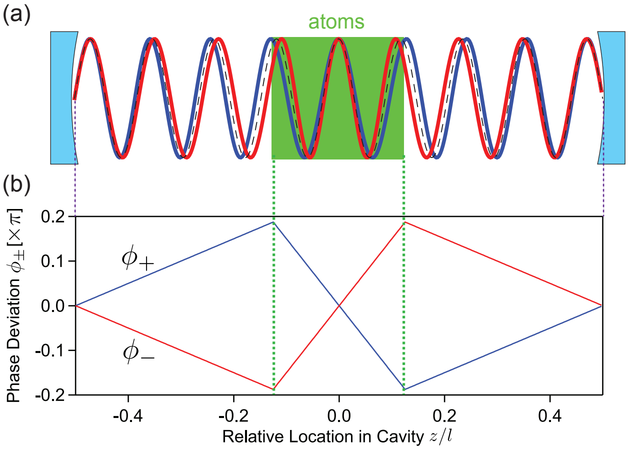

FIG. 12. (Color online) Illustration of the concept of spatial mode matching of the atoms-cavity modes. (a) In vacuum, the electric field of the higher frequency mode ω_+ (blue) has a shorter wavelength than the lower frequency mode ω_- (red), leading to a phase advance of the ω_+ mode relative to the ω_- mode as it advances from the left mirror to the left edge of the atomic medium (green). In the atomic medium, the refractive index $n_\pm$ at frequency $\omega_\pm$ is such that the ω_+ mode has a longer wavelength than the ω_- mode so that the two modes phase up in the middle of the cavity. For reference, the electric field for the bare cavity mode ω_c (dashed black) is shown. The phase mismatch in this illustration is deliberately made large by choosing $\Omega_\uparrow/2\pi = f_{\mathrm{FSR}}$. The length of the uniformly distributed atomic medium is set to $d = l/4$, again for illustration. (b) The spatial phase deviation $\phi_\pm$ of the $\omega_\pm$ modes from the empty cavity spatial phase. The red(blue) curves corresponding to ϕ_+ and ϕ_- respectively are used to generate the standing-wave modes in (a).

cavity axis evaluated for probe frequencies at the nominal resonance frequencies $\omega_\pm$ are

$$n_\pm(z) = 1 \mp \frac{\Omega_\uparrow}{4f_{\mathrm{FSR}}}\frac{1}{k_\pm}\rho_\uparrow(z)\,. \tag{28}$$

where $f_{\mathrm{FSR}} = c/2l$ is the cavity free spectral range, and $\rho_\uparrow(z)$ is the coarse-grained linear probability distribution function that an atom in $|\uparrow\rangle$ is located at z and normalized such that integrating over all of space yields 1. The coarse graining is performed over many lattice sites, and quantum fluctuations are ignored in this expression as they are a higher order effect.

As a first application, we assume the atoms uniformly fill a region of space of length d centered in the middle of the cavity of length l. In the atomic medium, the spatial phase deviation $\phi_\pm(z)$ of the standing-wave electric fields $\cos(\omega_c z/c + \phi_\pm)$ from the empty cavity spatial phase is given by

$$\phi_\pm(z) = \pm\frac{z\,\Omega_\uparrow}{4f_{\mathrm{FSR}}}\left(\frac{1}{l}-\frac{1}{d}\right) \quad \text{for } |\mathrm{z}| \leq \frac{\mathrm{d}}{2}. \tag{29}$$

In the limit of uniform filling $d = l$, the two probe modes are spatially matched, otherwise they acquire a differential spatial phase $\phi_+(z) - \phi_-(z)$ that grows linearly as z.

In the experiment of Ref. [1], the atoms were roughly Gaussian distributed along the cavity axis with standard deviation $\sigma_\rho = 0.84(9)$ mm, much less than the cavity length $l = 1.91$ cm. In this case, the spatial phase deviation of the standing-wave probe modes from the empty cavity spatial phase in the atomic medium is given by

$$\phi_\pm(z) = \pm\frac{\Omega_\uparrow}{4f_{\mathrm{FSR}}}\left(\frac{z}{l} - \frac{1}{2}\mathrm{Erf}\left(\frac{z}{\sqrt{2}\sigma_\rho}\right)\right)\,, \tag{30}$$

where $\mathrm{Erf}(\cdot)$ is the error function and $|z| \leq d/2$.

At $z = \sigma_\rho$, and typical $\Omega_\uparrow = 2\pi(300$ MHz), the differential probe spatial phase $\phi_+(z) - \phi_-(z)$ is expected to be only 31(3) mrad. Numerical simulations of the phase mismatch and projection noise show that this phase mismatch leads to $< 1\%$ reduction in the variance of the difference $\omega_+ - \omega_-$ relative to the variance in the same quantity for perfect spatial overlap of the two modes with one another.

F. Simultaneous mode probing at low light powers

We implemented two schemes to simultaneously measure the two modes of the vacuum Rabi splitting. The first is based on a modified Pound-Drever-Hall (PDH) scheme employing heterodyne detection to provide quantum-limited readout. The second technique is a heterodyne probe detection with full IQ quadrature measurement combined with active servoing of the optical path length.

1. *Heterodyne Pound-Drever-Hall detection*

The vacuum Rabi splitting is measured by sweeping the probe laser frequency and detecting the light reflected from the cavity input mirror. The resonance signals are extracted using a modified PDH detection scheme that employs optical heterodyne detection to achieve near photon-shot-noise-limited detection at probe powers of < 100 pW to several nW (see Fig. 13). To reduce sensitivity to laser and cavity noise, we measure both resonances ω_+ and ω_- simultaneously as discussed in Sec. IV C. The two probe components are generated by phase modulating the probe light to create sidebands at ± 151 MHz from the carrier. The modulation frequency is chosen to match the vacuum Rabi splitting of 302 MHz. Additional phase reference sidebands at ± 15.3 MHz are then imposed by a second phase modulator. To avoid degeneracy of the two probe components in the RF spectrum generated at the photodiode, the probe carrier is blue-shifted 52 MHz with respect to the reference heterodyne beam derived from the same laser as the probe.

The light reflected from the cavity is overlapped with the heterodyne light on a 90/10 beam splitter. Both beams are coupled into a single mode polarization-maintaining (PM) fiber to ensure high spatial mode

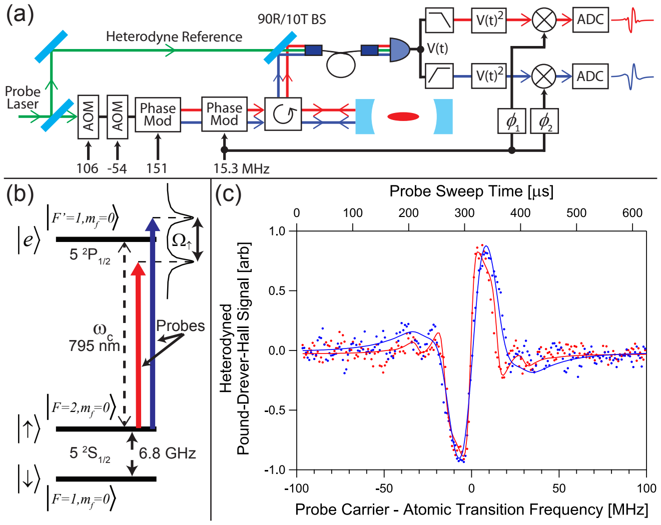

FIG. 13. (Color online) (a) Experimental setup of the heterodyne Pound-Drever-Hall (PDH) scheme used to probe the vacuum Rabi splitting. Both components of the vacuum Rabi splitting are simultaneously probed using the first order phase modulation sidebands generated by the first electro-optic modulator (EOM) and spaced ±151 MHz from the carrier. Additional ±15.3 MHz PDH phase reference sidebands are imposed by the second EOM. (b) Relevant energy level structure of ^{87}Rb. The bare cavity is made resonant with the $|\uparrow\rangle$ to $|e\rangle$ transition, and π-polarized probe light is used. (c) Simultaneous probing of the vacuum Rabi splitting. The blue and red points are the individual PDH error signals simultaneously measured by sweeping the phase-modulated probe laser frequency across the higher and lower frequency modes of the vacuum Rabi splitting respectively. The blue and red solid lines are curve fits to the data using an analytic model of the PDH error signal.

matching. The heterodyne laser power delivered to the photodiode is typically 0.8 mW. Working at low heterodyne powers provides additional immunity to classical intensity noise, as well as increased probe detection efficiency. The photodetector consists of a Hamamatsu S5973 photodiode, ac coupled to an Analog Devices AD8015 250 MHz transimpedance amplifier.

The two probe components are separated in the heterodyne RF spectrum using high and low pass filters, and notch filters at 99 MHz and 203 MHz. Each time-domain signal is squared using an Analog Devices AD835 250 MHz voltage multiplier. This step essentially mimics the square law detection of the photodiode that occurs in the usual PDH detection scheme. The resulting 15.3 MHz signals are then demodulated to dc. Figure 13(c) shows the resulting nearly simultaneously measured PDH error signals when the probe laser frequency is swept across a vacuum Rabi splitting. Linear fits to the central 15 μs of each probe component sweeping through resonance were used to extract the vacuum Rabi splitting $\Omega_\uparrow$.

Using this technique at low probe powers, we were able to measure the collective spin at a precision of 3.5(4) dB above the quantum projection noise level for an ensemble of $7.1(3) \times 10^5$ atoms with a calculated $m_s = 0.16$ photons/atom worth of free space scattering, directly proportional to photon recoil heating and loss of contrast as described in Sec. IV B. Simple extrapolation implies that with $\approx 2.2\times$ more probe photons, the measurement precision would reach the projection noise level while causing ≈ 0.35 photon/atom worth of free space scattering. This PDH probing technique suffers from added noised during the electronic squaring process, degrading the signal-to-noise. However, rather than further optimizing this approach, we chose to pursue a more sensitive readout scheme described in Sec. IV F 2 below.

2. *Heterodyne IQ detection*

For the results of Ref. [1], we employed heterodyne detection as described in Sec. IV F 1, but with the probe sidebands directly IQ demodulated so that the full amplitude and phase response during a frequency sweep could be used to extract the mode resonance frequencies, as described in Sec. II C. The probe beam was only phase modulated at 150 MHz; otherwise the rf configuration was the same as in Sec. IV F 1. The phase modulation generates a high frequency and a low frequency probe sideband, blue and red colored beams respectively in Fig. 14(a). To help remove optical path length noise in the heterodyne interferometer, we also detected the probe carrier and stabilized its phase measured at the photodiode using a servo loop with the 106 MHz acousto-optic modulator as the phase shifter.

We detect both the reflected and transmitted probe light and hence achieve better signal-to-noise in our symmetric cavity system as compared to just detecting only one port. Using IQ demodulators (Analog Devices ADL5387 for the high and low frequency probe sidebands, and Linear Technology LT5517 for the carrier), we phase coherently demodulate to obtain full amplitude and phase information of the probe electric field, or equivalently the full in-phase (I) and quadrature (Q) amplitudes. Figure 14(b) shows typical signals recorded in both reflection and transmission. The high (low) frequency probe component sweeps across the resonance ω_+ (ω_-), with the resulting signals shown in blue (red) in Fig. 14(b, c, d).

Phase stabilization is important for getting a good phase estimate for the IQ fit in reflection because the sweep spends relatively more time far from resonance than near resonance. Thus any phase wander of the heterodyne interferometer will show up as a phase wander of the reflected electric field. On the other hand, the phase stabilization is not crucial for the IQ transmission fit because there is no transmission off resonance, and therefore the signal is in the detection noise and has no well-defined phase anyway. However, the time to sweep across resonance needs to be fast compared to the timescale for phase wander so that the circle defined by the IQ transmission response does not rotate due to phase drift as

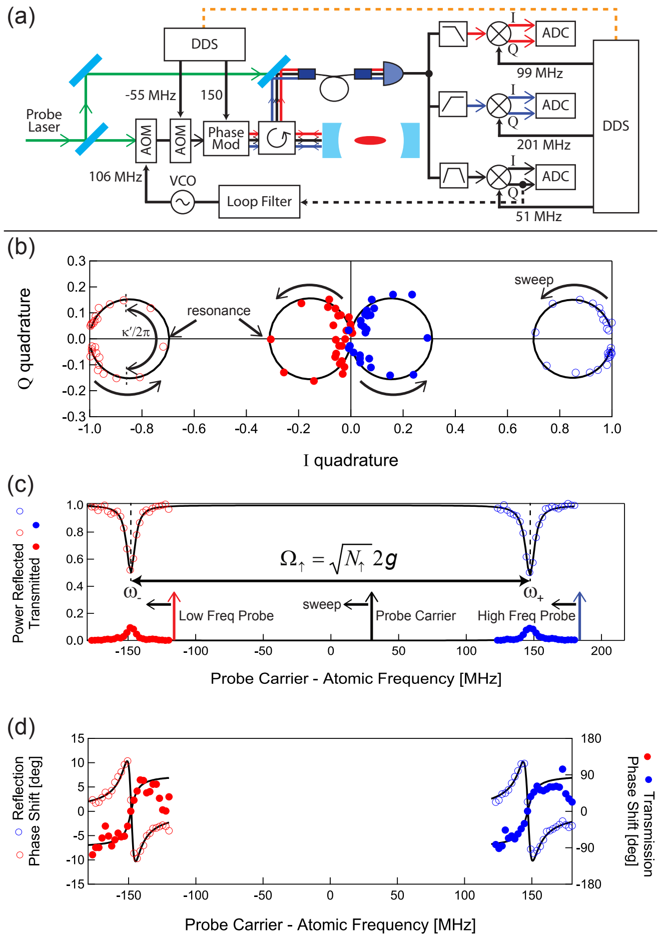

FIG. 14. (Color online) (a) Experimental setup of the heterodyne IQ detection scheme used to probe the vacuum Rabi splitting. Both components of the vacuum Rabi splitting are simultaneously probed using the first order phase modulation sidebands spaced ±150 MHz from the carrier. Probe transmission is also detected using a similar setup as the reflection detection (not shown). (b, c, d) Simultaneous probing of the vacuum Rabi splitting in transmission and reflection. The blue and red data points are the individual Rabi splitting signals simultaneously measured by sweeping the phase-modulated probe laser frequency. The resonance frequencies are extracted from fits (black curves) to the data plotted parametrically versus the probe frequency in the IQ plane (b). A rotation has been applied to align the circles along the I-quadrature for display purposes. The corresponding power $I^2 + Q^2$ (points – data, curve – from IQ fit results) (c), and phase shift $\arctan(Q/I)$ (points – data, curve – from IQ fit results) for both transmission and reflection (d).

the probe sweeps across resonance.

The resonance frequencies were extracted using least squares fitting in the IQ plane, yielding estimates $\Omega_\uparrow^{\mathrm{refl}}$ ($\Omega_\uparrow^{\mathrm{trans}}$) of the Rabi splitting from the IQ reflection (transmission) fit, respectively. Empirically, we find that the weighted average $(0.61\Omega_\uparrow^{\mathrm{refl}} + 0.39\Omega_\uparrow^{\mathrm{trans}})$ exhibited the least noise in two repeated measurements of the same Rabi splitting. This ratio reflects the relative quantum efficiencies in reflection and transmission. With an average number of missing probe photons in reflection (see Sec. II D) $M_m = 0.96(5) \times 10^5$ probe photons for a single measurement of $\Omega_\uparrow$, we achieve a probe measurement precision 6.5(5) dB below the projection noise level for $N_0 = 7.0(3) \times 10^5$ atoms obtained from the relative noise between two repeated $\Omega_\uparrow$ measurements on the same atomic ensemble.

In connection to the theory presentation in Sec. VI, we outline here the spectroscopic enhancement gained from the QND measurement in our experiment. The population difference and hence spin projection $J_z = (N_\uparrow - N_\downarrow)/2$ is determined from a measurement of $\Omega_\uparrow$, followed by a coherent swapping of populations between spin up and down using a microwave π-pulse, after which $\Omega_\uparrow$ is measured again. From repeated measurements of J_z, we observed a conditional spin noise reduction in the difference of two successive QND measurements $\Delta\left(J_z^{(2)} - J_z^{(1)}\right)$ of 2.6(3) dB below the projection noise level. By subtracting out probe measurement noise variance from the conditional spin noise variance, we inferred that a state with 4.9(6) dB reduced spin noise has been prepared. After the first measurement $J_z^{(1)}$, the measured contrast of the Ramsey fringe decreased from $\mathcal{C}_i = 0.97(1)$ before the measurement to $\mathcal{C}_f = 0.82(2)$. Taking into account the 1.5 dB loss of contrast, we concluded that a conditionally spin-squeezed state with spectroscopic enhancement 3.4(6) dB relative to the SQL has been prepared in an ensemble of $7.0(3) \times 10^5$ atoms .

V. QUANTUM BACK-ACTION LIMITS ON DETERMINING J_z

Having presented experimental examples of probing an atomic ensemble in the resonant limit near and below the quantum projection noise level in Sec. IV F, we now study the limitations on measurement resolution arising from Raman spin flips caused by free space scattering. We will begin by considering a simple three level model that will be used in Sec. VI to calculate spectroscopic enhancements relative to the SQL. The simple model will be extended in Sec. VII to probing the clock and cycling transitions in ^{87}Rb.

A. Average impact on J_z due to free space scattering

1. *Simple three-level model*

In this subsection, we consider how the free space scattering changes atomic population in the spin up and spin down two-level manifold through Raman or spin flip events. We define collective spin operators $\hat{J}_{x,y,z} = \sum_{i=1}^{N} \hat{J}^i_{x,y,z}$, where $\hat{J}^i_{x,y,z}$ is the single-atom spin operator for the ith atom such that $\hat{J}^i_z|\uparrow_i\rangle = \frac{1}{2}|\uparrow_i\rangle$, $\hat{J}^i_z|\downarrow_i\rangle = -\frac{1}{2}|\downarrow_i$

$\rangle$, etc. The collective spin operator is $\hat{J}_z = (\hat{N}_\uparrow - \hat{N}_\downarrow)/2$ where $\hat{N}_\uparrow$ and $\hat{N}_\downarrow$ are the atomic population operators defined in Sec. II A. Expectation values of the collective spin operators are denoted by $J_{x,y,z} \equiv \left\langle \hat{J}_{x,y,z} \right\rangle$. The collective Bloch vector is $\hat{\mathbf{J}} \equiv (\hat{J}_x,\, \hat{J}_y,\, \hat{J}_z)$. The radius of the collective Bloch sphere is $\mathcal{R} \equiv \sqrt{\left\langle \hat{\mathbf{J}}^2 \right\rangle}$. For arriving at the results presented in this section, only the atomic populations matter, and coherences are irrelevant.

A detailed accounting of all possible Raman scattering processes is required to make accurate predictions for a multi-level atom. We consider here the simplest model that captures the essential physics. In this toy model, the only states in the problem are the two-level system $|\uparrow\rangle$, $|\downarrow\rangle$ and the optical excited state $|e\rangle$, as described in Fig. 1(b). We assume that a free space scattering event causes an atom to spin flip from $|\uparrow\rangle$ to $|\downarrow\rangle$ via the intermediate state $|e\rangle$ with probability p. It is easy to see that the average change in the spin up population per photon scattered into free space is $dN_\uparrow/dM_s = -p$, and correspondingly $dJ_z/dM_s = -p$.

2. *Experimental verification of the average impact on J_z*

To connect with experiments performed in the resonant limit $\delta_c = 0$, where the Rabi splitting $\Omega_\uparrow = \sqrt{N_\uparrow}2g$ is measured directly rather than J_z, the previous result can be re-expressed as the change in the Rabi splitting per photon scattered as

$$\frac{d\Omega_\uparrow}{dM_s} = -p\frac{g}{\sqrt{N_\uparrow}}\,. \tag{31}$$

Accounting for the multi-level structure of ^{87}Rb and inhomogeneous coupling effects, we find in our system

$$\frac{d\Omega_\uparrow}{dM_s} = -\frac{7}{16}\frac{g}{\sqrt{N_\uparrow}}\,. \tag{32}$$

It is more convenient to measure the "missing" probe photons from the reflected port M_m than the multimode free-space-scattered photons M_s. The quantities are related by the following, using Eq. (11),

$$M_s = \frac{\Gamma}{\Gamma + \kappa - \kappa_1} M_m\,, \tag{33}$$

which evaluates to $M_s = 0.405(6) M_m$ for our system [1].

Experimentally, we observed a linear decrease in the Rabi splitting versus the "missing" photons M_m (see Fig. 15). From the slope $d\Omega_\uparrow/dM_m$, we inferred $M_s = 0.408(4) M_m$, confirming the rate equation analysis used in the derivation of Eq. (32).

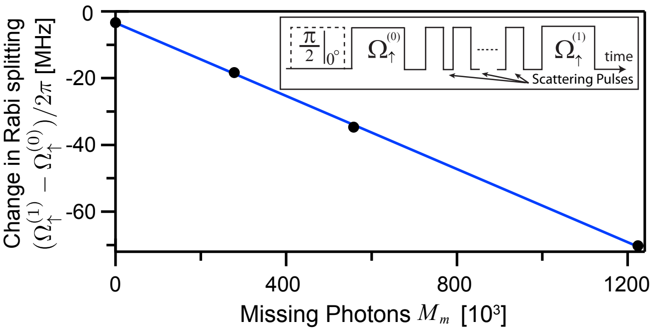

FIG. 15. (Color online) Measurement of change in Rabi splitting $(\Omega_\uparrow^{(1)} - \Omega_\uparrow^{(0)})/2\pi$ due to free space scattering versus the missing photons M_m in the reflected port. The slope is predicted to be $-\frac{7}{16}\frac{g}{\sqrt{N_\uparrow}}\frac{M_s}{M_m}$. Using the independently and accurately known values of $g = 2\pi(253$ kHz) and $N_\uparrow = 3.50(15) \times 10^5$, we inferred $M_s/M_m = 0.408(4)$, in excellent agreement with the theory prediction of 0.405(6). The inset shows the experimental sequence used to measure $\Omega_\uparrow^{(1)} - \Omega_\uparrow^{(0)}$. A CSS state is prepared using the $\pi/2$ pulse (dashed line), and then the first measurement $\Omega_\uparrow^{(0)}$ is made. Next, a variable number of probe pulses are applied to cause free space scattering, and M_m is measured. Finally, a second measurement $\Omega_\uparrow^{(1)}$ is made to determine $\Omega_\uparrow^{(1)} - \Omega_\uparrow^{(0)}$.

B. Measurement Resolution on J_z in Presence of Quantum Back-action

1. *Diffusion of J_z*

Free space scattering causes J_z to change on average by a certain amount, while the random nature of the spin flip process leads to a random walk or diffusion of the collective Bloch vector's spin projection J_z. Provided multiple scattering can be neglected, i.e. $p m_s \ll 1$, the diffusion process can be described by the relation

$$\frac{\left\langle (J_z(m_s) - J_z(0))^2 \right\rangle}{(\Delta J_{z,\mathrm{CSS}})^2} = 4\,p\,m_s\,, \tag{34}$$

with the spin flip probability setting the diffusion constant $4p$, and the random variable $J_z(m_s)$ describing the z-component of the Bloch vector after m_s scattering events per atom. The diffusion is normalized to the projection noise level for a CSS $(\Delta J_{z,\mathrm{CSS}})^2 = N/4$.

2. *Measurement imprecision due to photon shot noise*

The measurement imprecision $\Delta J_z^{\mathrm{meas}}$ is a weighted average of the state preparation variance or prior knowledge, and the probe vacuum noise:

$$\left(\frac{\Delta J_z^{\mathrm{meas}}}{\Delta J_{z,\mathrm{CSS}}}\right)^2 = \left(\frac{m_s}{m_s^{\mathrm{proj}}} + \frac{1}{\zeta_{\mathrm{prep}}}\right)^{-1}\,. \tag{35}$$

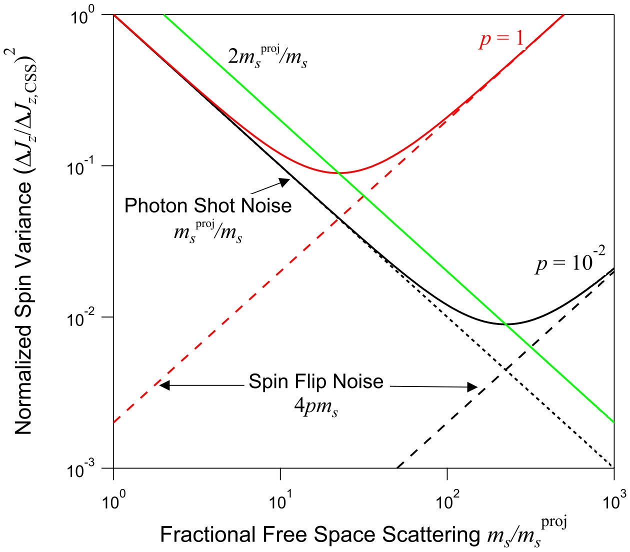

FIG. 16. (Color online) Normalized spin noise variance versus fractional free space scattering m_s/m_s^{proj}. The curves assume no prior knowledge, i.e., $\zeta_{\mathrm{prep}} \to \infty$, and $NC = 10^3$. The measurement variance decreases as $1/m_s$ from averaging down photon shot noise (dotted black line) until noise due to random spin flips (dashed red and black lines) takes over at large m_s. The minimum noise variance is $4\sqrt{pm_s^{\mathrm{proj}}} \to \sqrt{8p/NC}$ assuming perfect quantum efficiency and probing in the far-detuned limit. This minimum is reached when two noise contributions are equal at $m_s^{\mathrm{opt}} = \sqrt{m_s^{\mathrm{proj}}/4p} \to 1/\sqrt{8pNC}$ assuming perfect quantum efficiency and probing in the far-detuned limit. A larger collective cooperativity NC or lower spin flip probability p allows photon shot noise to be averaged down more before spin flip noise takes over, as illustrated by the two curves for $p/NC = 10^{-5}$ (black) and 10^{-3} (red). The locus of the minimum variance is $2m_s/m_s^{\mathrm{proj}}$ (green). Constructing an optimal Kalman filter to exponentially weight the measurement record at larger m_s more than at smaller m_s allows a factor of two improvement ($K = 2$) in the minimum noise variance to $\sqrt{2p/NC}$, a limit that is asymptotically approached.

The first term arises from the ability to split the resonance line due to photon shot noise, which scales as m_s^{-1}. The parameter $\zeta_{\mathrm{prep}} \equiv (\Delta J_{z,\mathrm{prep}}/\Delta J_{z,\mathrm{CSS}})^2$ characterizes the state preparation noise or prior knowledge relative to the projection noise level. For example, $\zeta_{\mathrm{prep}} = 1$ corresponds to preparing a CSS with no added technical noise, $\zeta_{\mathrm{prep}} \to \infty$ corresponds to preparing a state with essentially unknown J_z prior to measurement, and $\zeta_{\mathrm{prep}} < 1$ corresponds to a prepared state with reduced spin noise.

3. *Balancing measurement imprecision against diffusion of J_z*

Given the diffusion in J_z, and the photon shot noise in the probe, we must ask: How well can one measure J_z or equivalently the atomic population $N_\uparrow$? As a first pass, the total variance $(\Delta J_z')^2$ in the estimate of J_z is found by adding the measurement imprecision [Eq. (35)] and spin-flip-induced diffusion of J_z [Eq. (34)]:

$$\left(\frac{\Delta J_z'}{\Delta J_{z,\mathrm{CSS}}}\right)^2 = \left(\frac{m_s}{m_s^{\mathrm{proj}}} + \frac{1}{\zeta_{\mathrm{prep}}}\right)^{-1} + 4\,p\,m_s\,. \quad (36)$$

Averaging down photon shot noise determines the z-projection of the Bloch vector more and more precisely. Eventually, however, scattering-induced diffusion of J_z causes the value of J_z measured at earlier times to become less correlated with the value of J_z measured at later times, adding noise to the estimate of J_z, as shown in Fig. 16. The optimal resolution $\Delta J_z^{\mathrm{opt}}$ occurs at an optimal scattering m_s^{opt} where the noise contributions from measurement imprecision and diffusion due to Raman spin flips are equal:

$$m_s^{\mathrm{opt}} = \frac{1}{\sqrt{8pqNCh(\delta_c)}} - \frac{1}{\zeta_{\mathrm{prep}}}\frac{1}{2qNCh(\delta_c)}\,, \quad (37)$$

$$\left(\frac{\Delta J_z^{\mathrm{opt}}}{\Delta J_{z,\mathrm{CSS}}}\right)^2 = \frac{1}{K}\sqrt{\frac{8p}{qNCh(\delta_c)}}\frac{1}{A(\zeta_{\mathrm{prep}},\delta_c)}\,, \quad (38)$$

where the constant $K = 1$ in the present analysis, and $K = 2$ in an optimal Kalman filter analysis considered in Sec. V B 4. Unless otherwise stated, $K = 1$ is assumed for the rest of this paper including figures. The factor $A(\zeta_{\mathrm{prep}},\delta_c) = \frac{\zeta_{\mathrm{prep}}}{\zeta_{\mathrm{prep}} - \sqrt{p/2qNCh(\delta_c)}} \in [1, 2]$ is a small improvement due to including prior knowledge of the state. For $\zeta_{\mathrm{prep}} < \sqrt{2p/qNCh(\delta_c)}$, the optimal scattering m_s^{opt} goes to zero because we already have such good prior knowledge that measuring the state does more harm than good through introducing Raman scattering-induced spin-flips. The detuning dependence has been lumped into

$$h(\delta_c) = \left(\frac{\kappa}{\kappa'(\delta_c)}\frac{\omega(\delta_c)}{\sqrt{\delta_c^2 + \Omega_\uparrow^2}}\right)^2\,, \quad (39)$$

where $\kappa'(\delta_c)$ is the dressed cavity mode linewidth introduced in Eq. (8), $\omega(\delta_c)$ is the dressed cavity mode frequency introduced in Eq. (4), and $\Omega_\uparrow = \sqrt{N_\uparrow}2g$ is the collective vacuum Rabi splitting. The parameter $h(\delta_c^\circ) = 1/4$ at the critical detuning, and $h(\delta_c) \to 1$ as $|\delta_c| \to \infty$. In the limit of no prior knowledge $\zeta_{\mathrm{prep}} \to \infty$, no Kalman optimal filtering $K = 1$, and probing in the far-detuned limit, Raman spin flip noise limits the achievable resolution to $\left(\frac{\Delta J_z^{\mathrm{opt}}}{\Delta J_{z,\mathrm{CSS}}}\right)^2 = \sqrt{8p/qNC}$.

4. *Optimal Kalman estimator of J_z*

More rigorously, one can construct a Kalman filter to provide a minimum-mean-square-error estimator for J_z at the end of a continuous measurement record [23, 55, 56]. The measurement record is best parametrized by the average of free-space-scattered photons per atom m_s instead of time. Balancing between averaging down photon shot noise and increasing decorrelation due to spin flips, the optimal Kalman filter is a simple exponential de-weighting of the measurement record at smaller m_s relative to larger m_s. The exponential weighting time constant τ_W is given by the amount of time τ_W it takes for an average $m_s^W = \sqrt{m_s^{\mathrm{proj}}/4p} = 1/\sqrt{8pqNCh(\delta_c)}$ scattered photons per atom to occur; τ_W can be obtained from Eq. (16). The assumptions that the length of the measurement record is much longer than τ_W and that $m_s^W \ll 1$ have been made. In the Fourier domain, the filter is equivalent to a single-pole low-pass filter with corner frequency $\omega_K = 1/\tau_W$. Implementing the optimal Kalman filter improves the optimal estimate of J_z at the end of the measurement, increasing K in Eq. (38) from 1 to 2.

C. Single spin measurement resolution

Single spin resolution $\Delta J_z^{\mathrm{opt}} \leq 1/2$ is required for conditionally preparing states with spectroscopic sensitivity at the Heisenberg limit as well as the parity measurements needed for reading out NOON states, or Dicke states [57]. Single spin resolution in ensembles of ~ 100 ^{87}Rb atoms has recently been demonstrated using cavity-aided nondemolition measurements [46]. We find that in the far-detuned limit and with no prior knowledge, single spin resolution is reached for $p \leq \frac{qC}{8N}$, quantifying how ideal a cycling probe transition needs to be in order to resolve single spins. For $qC \sim 1$ and $N \sim 10^6$, one would need $p \leq 10^{-7}$, which is highly unrealistic for real multi-level level alkali-atoms due to off-resonant scattering from other hyperfine states, as will be discussed in Sec. VII for the case of ^{87}Rb. Alternatively, with high single atom cooperativity, $qC \geq 8Np$, single spin resolution could be attained without a cycling transition. For example, with $qC \sim 100$ and a worst-case open transition with $p = 1/2$, single spin resolution would be reached for $N \leq 25$ atoms.

VI. SPECTROSCOPIC ENHANCEMENT

Spectroscopic sensitivity refers to the ability to resolve the angle through which a Bloch vector or a Dicke state is rotated. To first approximation, the polar angular resolution is set by the conditional spin noise, discussed in Sec. V, and the radius $\mathcal{R}$ of the collective Bloch sphere on which the Bloch vector or Dicke state lives. In this section, we discuss how the radius $\mathcal{R}$ of the collective Bloch sphere is reduced by the measurement due to free space scattering, and derive the fundamental limits to the spectroscopic sensitivity. The radius $\mathcal{R}$ is proportional to the Ramsey contrast $\mathcal{C}$ for a CSS or a slightly spin-squeezed state. The radius is used here because it is possible to consider a conditional measurement with imprecision below a single spin. If all atoms remain in a superposition, the resulting state would be a fully symmetric Dicke state or eigenstate of the operator $\hat{J}_z$, with $\mathcal{R} = N/2$, but with $\left\langle \hat{\mathbf{J}} \right\rangle, \mathcal{C} = 0$. Nonetheless, Dicke states have near-Heisenberg limited spectroscopic sensitivity [58].

Enhanced sensitivity in one degree of angular resolution, say the polar angle θ, can be gained at the expense of enhanced uncertainty in an orthogonal degree of freedom, namely the azimuthal angle ϕ. For concreteness, the Bloch vector is initially prepared in a CSS along $\hat{x}$ with $\left\langle \hat{\mathbf{J}} \right\rangle = \hat{x}N/2$. The angular resolution of the polar angle for the CSS defines the SQL $\Delta\theta_{\mathrm{SQL}} = \Delta J_{z,\mathrm{CSS}}/\mathcal{R} = 1/\sqrt{N}$. If the actual angular resolution is $\Delta\theta$, then the metrologically relevant squeezing parameter is $\xi_m \equiv (\Delta\theta_{\mathrm{SQL}}/\Delta\theta)^2$ with $\xi_m \geq 1$ representing a spectroscopic enhancement in sensitivity that must arise from entanglement.

Angular resolution is reduced if the radius $\mathcal{R}$ of the collective Bloch sphere is reduced below its initial value without a corresponding decrease in the spin-noise. In the simplest model, each free-space-scattered photon from an atom in a superposition state leads to the collapse of its spin into spin up or down, leading to an average reduction in $\mathcal{R}$ by 1/2. If the free space scattering rate for each spin is unchanged by the scattering process, then the collective Bloch sphere radius normalized to its initial value $\widetilde{\mathcal{R}}$ as a function of the number of scattered photons per atom m_s is given by

$$\widetilde{\mathcal{R}} = e^{-m_s}\,. \tag{40}$$

Note that both Rayleigh and Raman scattering lead to a reduction in the collective Bloch sphere radius. In certain cases, free space Rayleigh scattering does not create wavefunction collapse [59], but this requires indistinguishability in the scattering process which reduces the information that can be extracted from the probe mode.

Putting Eq. 36 and Eq. 40 together, the spectroscopic enhancement is given by

$$\xi_m = \left(\frac{\Delta J_z'}{\Delta J_{z,\mathrm{CSS}}}\right)^{-2} e^{-2m_s}\,. \tag{41}$$

If Raman spin-flips dominate over Rayleigh scattering events, the optimal spectroscopic enhancement $\xi_m^{\mathrm{opt}} \sim \sqrt{qNC/p}$ is limited by spin-flip diffusion noise as considered in sub-section VI A. If Rayleigh scattering dominates, then the optimal spectroscopic enhancement $\xi_m^{\mathrm{opt}} \sim qNC$ is limited by shrinkage of the collective Bloch sphere radius $\mathcal{R}$, discussed in Sec. VI B. The change in the scaling of ξ_m^{opt} from $\sqrt{NC}$ in the Raman spin-flip limit to NC in the cycling transition limit allows far greater amounts of squeezing on a cycling transition. However, the loss of quantum efficiency q degrades squeezing as $\xi_m^{\mathrm{opt}} \sim q$ on a cycling transition, compared to the more

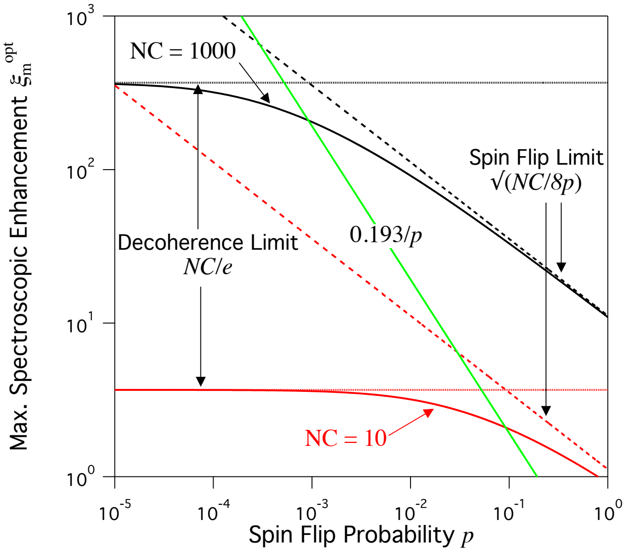

FIG. 17. (Color online) Optimal squeezing $\xi_m^{\rm opt}$ versus spin flip probability p for $NC = 1000$ (black curve) and $NC = 10$ (red curve) for probing in the far-detuned limit. Both curves take into account spin flip noise and decoherence. The curves assume perfect quantum efficiency $q = 1$ and no prior knowledge, i.e., $\zeta_{\rm prep} \to \infty$. The decoherence-limited squeezing $\xi_m^{\rm opt} = NC/e$ (dotted lines) is approached for $p \ll e^2/8NC$, and the spin-flip-limited squeezing $\xi_m^{\rm opt} = \sqrt{NC/8p}$ (dashed lines) is approached for $p \gg e^2/8NC$. The locus of optimal squeezing at the crossover point $p = e^2/8NC$ is $0.193/p$ (green line).

favorable scaling $\xi_m^{\rm opt} \sim \sqrt{q}$ in the Raman spin-flip limited regime.

A. Small decoherence/spin flip limit

Here we consider the case where the reduction in the radius $\mathcal{R}$ of the collective Bloch sphere may be ignored. This is justified if the optimal scattering $m_s^{\rm opt}$ that optimizes the measurement resolution of J_z is small, $m_s^{\rm opt} \ll 1$, equivalently $pqNC\,(\kappa/\Gamma)^2 \gg 1$ for probing in the far-detuned limit. In this regime, the radius $\widetilde{\mathcal{R}}$ remains approximately 1, so that the spectroscopic enhancement is primarily set by the reduction in the spin noise, discussed previously in Sec. V

$$\xi_m^{\rm opt} \approx \left(\frac{\Delta J_z^{\rm opt}}{\Delta J_{z,{\rm CSS}}}\right)^{-2}, \tag{42}$$

where $\left(\frac{\Delta J_z^{\rm opt}}{\Delta J_{z,{\rm CSS}}}\right)^2$ has been introduced in Eq. 38. In the limit of no prior knowledge $\zeta_{\rm prep} \to \infty$ and probing in the far-detuned limit, Raman spin flip noise limits the achievable squeezing to $\xi_m^{\rm opt} = \sqrt{qNC/8p}$.

B. Large decoherence/cycling transition limit

Here we consider the case where the reduction in the radius $\mathcal{R}$ of the collective Bloch sphere plays an important role in determining the angular resolution. If the probing is performed on a nominally closed transition where Raman scattering spin-flips due to probe polarization imperfections and off-resonant scattering are very improbable, spin-flip diffusion noise is negligible and the only limit to spectroscopic enhancement is the shrinking of the radius $\mathcal{R}$ due to free space (Rayleigh) scattering. The probing is performed in the large decoherence or cycling transition regime when the optimal scattering $m_s^{\rm opt}$ that optimizes the measurement resolution of J_z is not small. Formally, this regime occurs when the optimum spectroscopic enhancement calculated from Eq. (42) is $\xi_m^{\rm opt} \geq 0.193/p$.

In the large decoherence regime, the spectroscopic enhancement is given by $\xi_m = \frac{m_s}{m_s^{\rm proj}} e^{-2m_s}$, ignoring the small improvement that may result from prior knowledge. An optimum is reached when the radius $\widetilde{\mathcal{R}}$ is reduced by 2 or equivalently $m_s^{\rm opt} = 1/2$, yielding an optimum $\xi_m^{\rm opt} = 1/(2e\, m_s^{\rm proj})$. In the far-detuned limit, the optimal squeezing $\xi_m^{\rm opt} \to qNC/e$. We caution that the simple model presented here is not valid near the Heisenberg limit because while measurement resolution below a single spin may be achieved, the effective spin noise variance must be clamped to 1/4 in order to enforce the Heisenberg limit on spectroscopic sensitivity.

VII. OPTIMAL SQUEEZING FOR ^{87}Rb

Using the framework above, we now analyze the limits of two separate probing schemes. From Sec. III, we have shown that the measurement resolution at fixed free space scattering improves with cavity detuning δ_c, but ultimately saturates to a value set by the collective cooperativity parameter NC. For squeezing on a clock transition comprised of two hyperfine ground states, the maximal detuning is approximately half of the ground state hyperfine splitting $\delta_c = \omega_{\rm hf}/2$. We are interested in the ultimate limits of squeezing in such a system, taking into account Raman spin flips and decoherence. Motivated by the fact that Raman spin flips limit the achieveable squeezing on a hyperfine clock transition, we then analyze squeezing on a cycling transition, where Raman spin flips are greatly reduced, but introduce an additional scaling with δ_c, resulting in a region of saturation of the spectroscopic enhancement as NC is increased. In both scenarios, the ratio $\omega_{\rm hf}/\Gamma$ of the hyperfine splitting to the excited state decay linewidth plays a critical role.

A. Optimal squeezing via differential measurement of ^{87}Rb clock transition

We now consider the measurement scheme demonstrated by the MIT group [7] in which the pseudospin states were as in Ref. [1], namely the clock states of ^{87}Rb $|\uparrow\rangle \equiv |5^2S_{1/2}, F=2, m_F=0\rangle$ and $|\downarrow\rangle \equiv |5^2S_{1/2}, F=1, m_F=0\rangle$. The bare cavity frequency is tuned to the average of the two ground states to optically excited state transitions near 780 nm. This tuning ensures that an atom in $|\downarrow\rangle$ shifts the dressed cavity resonance frequency by an equal, but opposite amount as an atom in $|\uparrow\rangle$. The excited state hyperfine splitting ~ 500 MHz is much less than the ground hyperfine splitting and is taken to be zero for the following analysis.

The problem is analyzed by extending the linearized two-mode model of Eq. (5) to a linearized three-mode model in which the atomic operator $\hat{a}$ is generalized to operators $\hat{a}_\downarrow$ and $\hat{a}_\uparrow$ to yield three coupled differential equations, along with the same input-output relations given by Eq. 7:

$$\begin{aligned}
\frac{d\langle\hat{c}\rangle}{dt} &= -\frac{1}{2}\kappa\langle\hat{c}\rangle - \imath g\left(\sqrt{N_\uparrow}\langle\hat{a}_\uparrow\rangle - \sqrt{N_\downarrow}\langle\hat{a}_\downarrow\rangle\right) + \sqrt{\kappa_1}c_i\,,\\
\frac{d\langle\hat{a}_\uparrow\rangle}{dt} &= -\frac{1}{2}\left(\Gamma + \imath\,\omega_{\rm hf}\right)\langle\hat{a}_\uparrow\rangle - \imath\sqrt{N_\uparrow}g\langle\hat{c}\rangle\,,\\
\frac{d\langle\hat{a}_\downarrow\rangle}{dt} &= -\frac{1}{2}\left(\Gamma - \imath\,\omega_{\rm hf}\right)\langle\hat{a}_\downarrow\rangle - \imath\sqrt{N_\downarrow}g\langle\hat{c}\rangle\,. \qquad (43)
\end{aligned}$$

The equations are now written in a rotating frame at the bare cavity resonance frequency that is chosen such that the two optical atomic transitions are detuned by $\pm\omega_{\rm hf}/2$. The rate of scattering into free space is described by the two field amplitudes $a_{s,\uparrow,\downarrow} = \sqrt{\Gamma}\langle\hat{a}_{\uparrow,\downarrow}\rangle$ and normalized such that the rate of photons scattered into free space is simply $\dot{M}_s = |a_{s,\uparrow}|^2 + |a_{s,\downarrow}|^2$.

From the coupled set of Eq. (43), we find that the rms phase shift of the transmitted light field caused by the rms projection noise level fluctuation in the population difference is:

$$\Delta\phi^{\rm proj} = \sqrt{N}C\left(\frac{\Gamma}{\omega_{\rm hf}}\right)\left(\frac{1}{1+NC\Gamma^2/\omega_{\rm hf}^2}\right)\,. \qquad (44)$$

This expression assumes the damping rates are small $\kappa, \Gamma \ll \omega_{\rm hf}, \sqrt{N/2}\,2g$. The phase shift initially climbs with increasing atom number as $\sqrt{N}$, but saturates to a maximum value $\Delta\phi^{\rm proj} = \sqrt{C}/2$ at a critical atom number given by $NC = (\omega_{\rm hf}/\Gamma)^2$, after which the phase shift decreases as $1/\sqrt{N}$. The physical interpretation for this decrease is that above the critical atom number, the dressed cavity mode linewidth κ' rapidly starts to broaden with increasing atom number. The number of free-space-scattered photons required to resolve the projection noise level phase shift of the probe is

$$m_s^{\rm proj} = \frac{1}{4qNC}\left(1 + NC\left(\frac{\Gamma}{\omega_{\rm hf}}\right)^2\right)\,. \qquad (45)$$

The diffusion of the difference between the estimate of J_z and the actual value of J_z is driven by Raman transitions that move atoms from $|\uparrow\rangle$ to $|F=1\rangle$ or $|\downarrow\rangle$ to $|F=2\rangle$. Raman transitions between states of the same F (i.e., $\Delta F = 0$) lead to loss of coherence, but do not change the coupling of the atom to the cavity mode in the limit where the excited state hyperfine splitting is neglected, as we do here. Hyperfine changing transitions $\Delta F \neq 0$ cause the detuning to change sign, but not magnitude, making such a process equivalent to a spin flip. Accounting for transition branching ratios, we find that to a good approximation, we can apply Eq. (36), with an effective spin flip probability $p = 1/6$. Assuming the loss of coherence is small, then the optimal spectroscopic enhancement with respect to average probe photon number is

$$\xi_m^{\rm opt} = \frac{\sqrt{6qNC}}{1 + 4NC\Gamma^2/\omega_{\rm hf}^2}\,. \qquad (46)$$

At small N, the spectroscopic enhancement scales as $\sqrt{6qNC}$, reaching a peak value of $\xi_m^{\rm opt} = \sqrt{3q/8}\,\omega_{\rm hf}/\Gamma$ at a value $NC = \frac{1}{4}(\omega_{\rm hf}/\Gamma)^2$, slightly before the maximum phase shift is reached. At larger NC, the spectroscopic enhancement scales as $\xi_m^{\rm opt} = \sqrt{3q/8NC}(\omega_{\rm hf}/\Gamma)^2$.

Taking the quantum efficiency to be $q = 1$, the maximum spectroscopic enhancement for ^{87}Rb is quite large at 28 dB. The exact details of the full measurement sequence (i.e., whether rotations such as π-pulses are used to cancel sources of technical noise as was done in Refs. [1, 7]) are needed to construct an optimal estimator of J_z, but, at best, a 3 dB further improvement may result.

Because C does not depend on the cavity length, the optimum N for peak spectroscopic enhancement scales as $(w_0^2/F)(\omega_{\rm hf}/\Gamma)^2$, where w_0 is the cavity mode waist, and F is the cavity finesse. More fundamentally, no change in the cavity geometry (w_0 and l) or finesse F changes the maximum obtainable enhancement in spectroscopic sensitivity. This enhancement is determined solely by the atomic properties. Figure. 18 shows the spectroscopic enhancement versus atom number for a range of technologically feasible cavity finesses.

Resolving very small phase deviations or small frequency shifts imposes technical challenges that are modified with cavity geometry or finesse, as shown by the probe frequency (Fig. 19) and probe phase shift (Fig. 20) resolutions required to obtain the spectroscopic sensitivities shown in Fig. 18. All three figures assume the cavity geometry of Ref. [1], $l = 1.91$ cm and $w_0 = 71$ μm. Finally, we note that Fig. 19 shows the technical requirement on probe frequency resolution is more relaxed above the optimum N compared to achieving the same spectroscopic enhancement at a value below the optimum N.

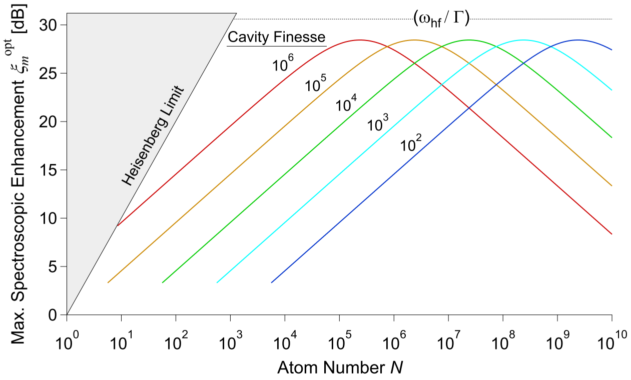

FIG. 18. (Color online) The fundamental optimum spectroscopic enhancement for differential probing of the ^{87}Rb clock transition, as performed in Ref. [7]. The calculations assume a net quantum efficiency of $q = 1$ and the cavity geometry described in the text and Ref. [1]. The purple, light blue, green, orange, and red curves correspond to cavity finesses of $F = 10^2, 10^3, 10^4, 10^5$, and 10^6, respectively. All these finesses are experimentally feasible. The atom number N at which the spectroscopic enhancement is maximized scales with the cavity mode waist w_0 and cavity finesse F as w_0^2/F.

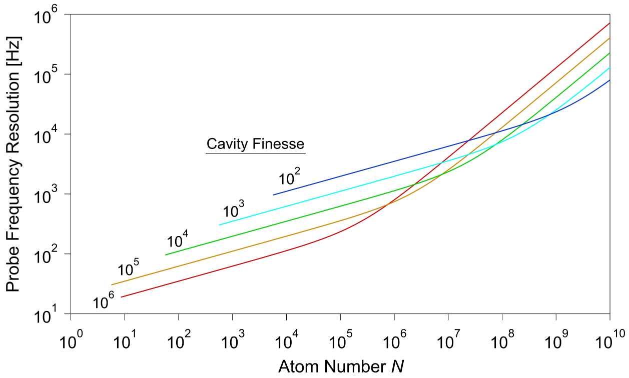

FIG. 19. (Color online) Frequency resolution with which the relative frequency of the probe and dressed cavity mode must be measured to obtain the spectroscopic enhancements shown in (and under the same conditions as) Fig. 18 . The purple, light blue, green, orange, and red curves correspond to cavity finesses of $F = 10^2, 10^3, 10^4, 10^5$, and 10^6, respectively.

B. Optimal squeezing on ^{87}Rb cycling transition

Having seen that the optimal squeezing on a clock transition is fundamentally limited by Raman spin flips, we consider a situation in which Raman spin flips are reduced, namely probing on a cycling transition, and show that larger amounts of squeezing are possible in this configuration than on the clock transition [46, 60].

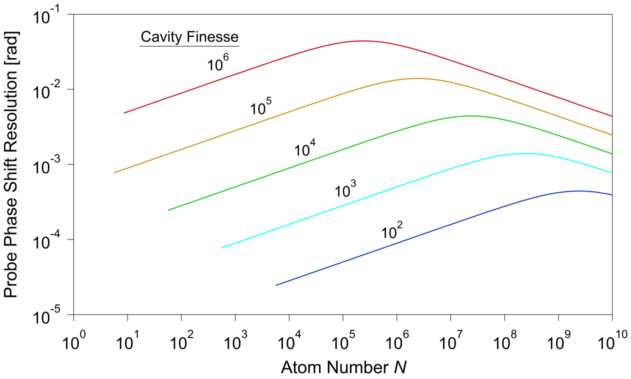

FIG. 20. (Color online) Phase resolution with which the transmitted probe light must be measured to obtain the spectroscopic enhancements shown in (and under the same conditions as) Fig. 18. The purple, light blue, green, orange, and red curves correspond to cavity finesses of $F = 10^2, 10^3, 10^4, 10^5$, and 10^6, respectively.

As a concrete example of how a cycling transition can be used to enhance probing, we consider the cycling transition in ^{87}Rb, $|\uparrow\rangle \equiv |F = 2, m_F = 2\rangle$ to $|e\rangle \equiv |F = 3', m_F = 3\rangle$ at wavelength 780 nm. The spin down state is chosen as $|\downarrow\rangle \equiv |F = 1, m_F = 1\rangle$. For the following, the probing scheme with relevant energy levels, dipole matrix elements, decay branching ratios, dressed mode frequencies, and probe laser detunings are shown and defined in Fig. 21. Here we will extend the previous models of the precision of the estimation of J_z and the loss of signal due to wavefunction collapse to capture the essential physics for this system. Key results are that there exists a region of saturation, or universal spectroscopic enhancement, set only by atomic properties and in which varying atom number and cavity finesse can have little impact. However, unlike in the previous section, the asymmetry in the cavity coupling to $|\uparrow\rangle$ and $|\downarrow\rangle$ allows this saturation region to be surpassed at large values of NC.

We must first consider what limits the rate of Raman scattering processes that can lead to diffusion of the spin projection J_z. The probe polarization can be set to pure σ^+ to better than 10^{-4}, so that Raman scattering from $|\uparrow\rangle$ is suppressed to at least this level or greater. The more fundamental Raman scattering limitation arises from the finite hyperfine splitting $\omega_{\text{hf}} = 2\pi \times (6834\text{ MHz})$. Specifically, atoms in $|\downarrow\rangle$ can non-resonantly Raman scatter probe photons from $|e'\rangle \equiv |F = 2', m_F = 2\rangle$.

In the following discussion, the quantity m_s is importantly defined as the average number of probe photons (normalized to the total atom number) Rayleigh scattered into free space by atoms in $|\uparrow\rangle$. All other scattering processes will be scaled from this quantity using the quantities defined in Fig. 21. The key parameters for rescaling are the ratio of the dipole matrix elements $r = M_{\downarrow e'}/M_{\uparrow e} = 1\sqrt{2}$, the decay branching ratio $B_{3e'} = 1/6$ from $|e'\rangle$ to $|3\rangle \equiv |F = 2, m_F = 1\rangle$, and the detunings of the probe light δ_e and $\delta_{e'} = \delta_e - \omega_{\text{hf}} - \omega_{\text{ehf}}$ from resonance with the transitions $|\uparrow\rangle \rightarrow |e\rangle$ and $|\downarrow\rangle \rightarrow |e'\rangle$ respectively. As in the previous section, we neglect the excited state hyperfine splittings so that $\delta_{e'} \approx \delta_e - \omega_{\text{hf}}$.

The rms imprecision in the estimate of J_z relative to

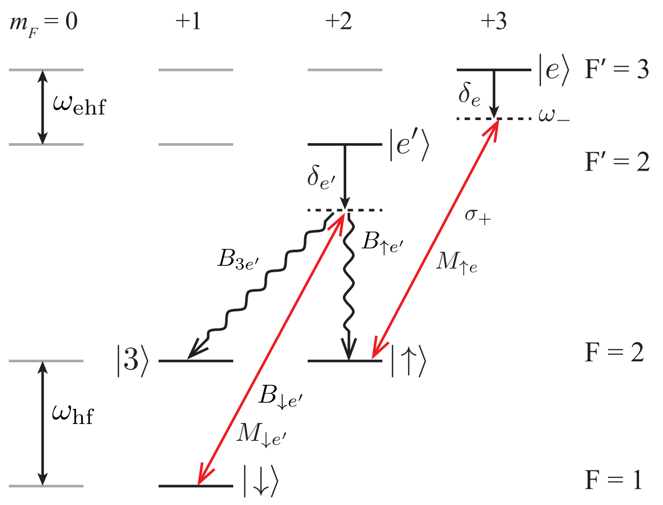

FIG. 21. (Color online) Probing scheme for the cycling transition in ^{87}Rb. The ground hyperfine states $F = 2$ and $F = 1$ are split by $\omega_{\mathrm{hf}} = 2\pi \times (6834\text{ MHz})$. The values of m_F are labeled across the top. The relevant $F' = 3$ and $F' = 2$ excited D2 transitions at wavelength 780 nm are also shown with the excited state splitting $\omega_{\mathrm{ehf}} = 2\pi \times (267\text{ MHz})$. The pseudo spin-1/2 system is here composed of $|\uparrow\rangle = |F = 2, m_F = 2\rangle$ and $|\downarrow\rangle = |F = 1, m_F = 1\rangle$. Ideally, the σ^+-polarized probing laser couples only $|\uparrow\rangle$ to the optically excited state $|e\rangle$ with dipole matrix element $M_{\uparrow e}$ at a frequency detuning δ_e that is approximately equal to the dressed-cavity mode frequency ω_-. In this illustration, δ_e is negative. By dipole selection rules, $|e\rangle$ can only decay back to $|\uparrow\rangle$. However, the same probe laser also couples $|\downarrow\rangle$ to the single excited state $|e'\rangle$ with dipole matrix element $M_{\downarrow e'}$ and larger detuning from resonance $\delta_{e'} = \delta_e - \omega_{\mathrm{hf}} - \omega_{\mathrm{ehf}}$. The ratio of matrix elements is $M_{\downarrow e'}/M_{\uparrow e} = 1/\sqrt{2}$. Finally, the state $|e'\rangle$ decays to states $|\downarrow\rangle$, $|\uparrow\rangle$, and $|3\rangle$ with fractional branching ratios $B_{\downarrow e'} = 1/2$, $B_{\uparrow e'} = 1/3$, and $B_{3e'} = 1/6$ respectively.

the projection noise level can be approximately modeled as

$$\left(\frac{\Delta J_z}{\Delta J_{z,\mathrm{CSS}}}\right)^2 = 4p_\uparrow m_s + p_3 m_s + \frac{\widetilde{m}_s^{\mathrm{proj}}}{m_s}\,. \tag{47}$$

Starting in order of physical significance, the first and second terms arise from diffusion of J_z caused by Raman transitions from $|\downarrow\rangle \to |\uparrow\rangle$ and $|3\rangle$ with effective probabilities $p_\uparrow$ and p_3 given approximately by

$$p_{\uparrow,3} = B_{\uparrow,3\ e'} r^2 \left(\frac{\delta_e}{\delta_{e'}}\right)^2 . \tag{48}$$

In this simple treatment, Raman decays to $|3\rangle$ are treated as loss, as reflected in the smaller numerical pre-factor in front of the second term of Eq. (47).

The third term in Eq. (47) is modified to reflect that both states can interact with the probe at large detunings such that the dressed cavity mode frequency is less sensitive to quantum projection noise in J_z, and thus more probe photons must be used to resolve J_z at the projection noise level, i.e.,

$$\widetilde{m}_s^{\mathrm{proj}} = \frac{m_s^{\mathrm{proj}}}{R_{\mathrm{ray}}}\ . \tag{49}$$

Here, m_s^{proj} is defined by Eqs. (18), (8), and (4). Indistinguishability is accounted for by

$$R_{\mathrm{ray}} = \left(1 - r\frac{\delta_e}{\delta_{e'}}\right)^2\ . \tag{50}$$

Note that $R_{\mathrm{ray}} \leq 1$ with an asymptotic value of $R_{\mathrm{ray}} \to 1$ at large detunings.

There are two effects that are neglected in Eq. 49 by first assuming they are small, and then verifying this to be the case after the calculations. First, in applying the dressed cavity linewidth result for κ' from Eq. (8), we assume that the cavity mode is negligibly further broadened by atoms in state $|\downarrow\rangle$. By estimating the additional broadening evaluated at the optimal cavity detuning and average number of scattered photons, we find that the optimal spectroscopic enhancements calculated in Fig. 22 are reduced by < 0.3 dB due to the neglected mode broadening. Second, we assume that the dressed mode frequency ω_- calculated from Eq. (4) is only modified by a small fraction by atoms in state $|\downarrow\rangle$. Again, this assumption is verified to be the case at the optimal cavity detuning and the average number of scattered photons, with the exception of the case where $N > 10^8$ and cavity finesse $F = 100$, as shown in Fig. 22 where several dB of deviations are possible due to this effect.

Next, we consider how collapse due to free space scattering reduces the radius of the collective Bloch sphere, specifically

$$\widetilde{\mathcal{R}} = e^{-m_s(R_{\mathrm{ray}}+R_{\mathrm{ram}})}\,, \tag{51}$$

where the partial cancellation of wavefunction collapse due to indistinguishable Rayleigh scattering off of both $|\uparrow\rangle$ and $|\downarrow\rangle$ (see [59]) is accounted for by R_{ray}.

The term R_{ram} accounts for Raman scattering from $|\downarrow\rangle$ to $|3\rangle$.

$$R_{\mathrm{ram}} = B_{3e'} r^2 \left(\frac{\delta_e}{\delta_{e'}}\right)^2\ . \tag{52}$$

As before, we assume that Raman scattering to state $|3\rangle$ is equivalent to atom loss. Note also that $R_{\mathrm{ram}} \leq B_{3e'} r^2$.

Equations (47)-(52) are used to numerically estimate the optimal spectroscopic enhancement ξ_m^{opt} shown versus atom number N in Fig. 22 for a range of technologically reasonable cavity finesses and assuming the cavity geometry of Ref. [1] (cavity length $l = 1.91$ cm, mode waist size $w_0 = 71\ \mu$m), and perfect quantum efficiency $q = 1$. The optimization is done with respect to both m_s and the dressed cavity mode frequency ω_- (tuned by changing the bare cavity frequency). The mode frequency ω_- at the optimum is shown in Fig. 23. The loss of signal due to wavefunction collapse and scattering to $|3\rangle$ at the optimum is shown in Fig. 24.

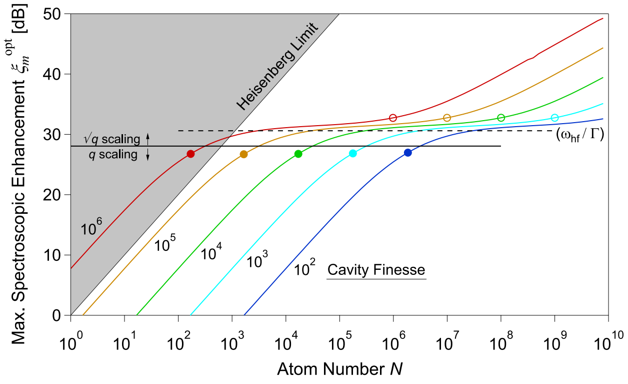

FIG. 22. (Color online) Theoretical optimal spectroscopic enhancement ξ_m^{opt}(solid curves) in dB relative to the SQL versus total ^{87}Rb atom number N for the current cavity geometry of Ref. [1] and probing near the D2 cycling transition as shown in Fig. 21. The optimization is performed for a range of technically realizable cavity finesses $F = 10^2, 10^3, 10^4, 10^5$, and 10^6 (blue, cyan, green, yellow, and red curves respectively) under the assumption of perfect quantum efficiency $q = 1$. Note the unphysical regime below the Heisenberg limit (disallowed grey region). A region of saturation of ξ_m^{opt} versus N occurs near $\xi_m^{\text{opt}} \approx \omega_{\text{hf}}/\Gamma$ shown by the labeled horizontal dashed line. The physical origin for the saturation region arises from competition between the scaling of the off-resonance Raman scattering probabilities and the dressed cavity mode broadening, as described in the text. The points of 3 dB deviation from NC scaling at low atom number (solid circles) and $\sqrt{NC}$ scaling at large atom number (open circles) occur when the solid curves cross $\xi_m^{\text{opt}} = 27$ dB and 33 dB, respectively. The approximate transition from q to $\sqrt{q}$ scaling occurs when the solid curves cross $\xi_m^{\text{opt}} = 28$ dB, the point at which the scaling is approximately $q^{3/4}$.

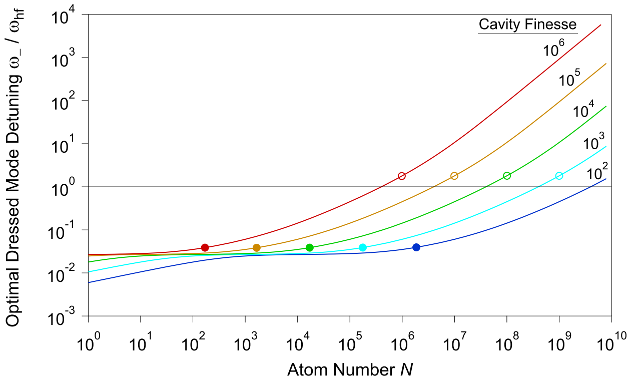

FIG. 23. (Color online) The dressed mode frequency ω_- that optimizes the spectroscopic enhancement ξ_m for the conditions described in Fig. 22, where again the cavity finesses $F = 10^2, 10^3, 10^4, 10^5$, and 10^6 correspond to blue, cyan, green, yellow, and red curves, respectively. The open and closed circles indicate the locations of the 3 dB points in Fig. 22. The mode frequency is normalized to the hyperfine splitting $\omega_{\text{hf}}/2\pi = 6.834$ GHz. Note that $\omega_- \approx \Gamma$ at $\omega_-/\omega_{\text{hf}} \approx 10^{-3}$. Comparing to Fig. 22, one finds that the transition to spectroscopic enhancement scaling as $\xi_m^{\text{opt}} \propto \sqrt{qNC}$ occurs near $\omega_- \sim 1.8 \times \omega_{\text{hf}}$. Above this point, the spin flip probabilities $p_{\uparrow,3}$ change little with ω_-.

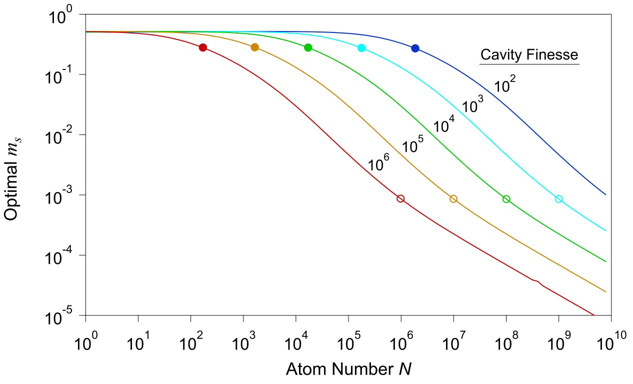

FIG. 24. (Color online) The scattering m_s that optimizes the spectroscopic enhancement ξ_m^{opt} shown in Fig. 22. Again, the cavity finesses $F = 10^2, 10^3, 10^4, 10^5$, and 10^6 correspond to the solid blue, cyan, green, yellow, and red curves, respectively. The open and closed circles indicate the locations of the 3 dB points in Fig. 22. Comparing to Fig. 22, one finds that the transition to spectroscopic enhancement scaling as $\xi_m^{\text{opt}} \propto qNC$ occurs when $m_s \approx 0.25$, indicating that at larger N, far off-resonance Raman scattering begins to create significant diffusion of J_z that limits the precision of the estimation of J_z as discussed in the main text.

At low atom number, the spectroscopic enhancement scales as $\xi_m^{\text{opt}} \sim qNC$. At high atom number, the spectroscopic enhancement scales as $\xi_m^{\text{opt}} \sim \sqrt{qNC}$. There is an intermediate region of atom number for which the spectroscopic enhancement is relatively flat versus atom number with $\xi_m^{\text{opt}} \sim \omega_{\text{hf}}/\Gamma$. The physical origin of this plateau arises from the form of the critical detuning of Eq. (20).

In the good cavity limit, the scattering necessary to reach projection noise level sensitivity m_s^{proj} falls as $1/\delta_c^4$ for $\delta_c < \delta_c^\circ$, making it beneficial to operate with $|\omega_-| \sim \delta_c \geq \Gamma\sqrt{NC/q}$. However, the Raman transition probabilities $p_{\uparrow,3}$ continue to grow quadratically with the detuning, while detuning farther no longer rapidly reduces m_s^{proj}.

Assuming the critical detuning δ_c° is optimal for the reasons above, and in the limit of $|\omega_-| < \omega_{\text{hf}}$, the Raman transition probabilities scale as $p_{\uparrow,3} \sim (NC/q)(\Gamma/\omega_{\text{hf}})^2$, while $m_s^{\text{proj}} \sim 1/qNC$. Optimizing the total noise in our estimate of J_z using Eq. (47) with respect to m_s reproduces the observed plateau value $\xi_m^{\text{opt}} \sim \omega_{\text{hf}}/\Gamma \sim 10^3$. The plateau region is exited at low atom number when loss of signal [described by Eq. (51)] dominates the reduction in spectroscopic enhancement, as illustrated by the loss of signal due to wavefunction collapse shown in Fig. 23. At high atom number, the plateau region is exited when the optimum mode frequency becomes large compared to the hyperfine splitting $|\omega_-| > \omega_{\text{hf}}$, as shown in Fig. 24.

Importantly, this analysis shows that there is a range in which increasing either finesse or atom number can have little effect on the optimal spectroscopic enhancement achieved. Also, note that the value of the plateau does not depend on the cavity geometry, and therefore represents a universal value that depends only on the atomic properties. One can also show that the range of atom number spanned by the plateau and the position of the first corner scales roughly as $N \sim w_0^2/F$, but does not depend on the cavity length l. Finally, for atom numbers below 10^3, it appears possible to both prepare and readout states near the Heisenberg limit using this approach and technologically feasible cavity finesses. Indeed, Ref. [46] recently demonstrated single atom measurement resolution for $N \sim 100$ using the approach described here.

VIII. COHERENT REINITIALIZATION FOR REDUCED RECOIL HEATING

In this final brief section, we consider whether coherence preserving quantum non-demolition measurements can also be used to reduce the total photon-recoil heating in a Ramsey spectroscopy measurement cycle. A low number of photon recoils imparted in a complete experimental cycle, not just the readout, would allow neutral atom traps to operate more like ion traps, with their advantages of high duty cycle and high repetition rates. We use the canonical example of Ramsey spectroscopy to show how low photon recoil in a complete experimental cycle can be achieved. Imagine reading out the Bloch vector projection J_z at the end of a Ramsey sequence with a QND measurement at or below the projection noise limit. If one were to repeat the experimental cycle by optically repumping all the atoms back into $|{\downarrow}\rangle$, each atom in the ensemble would experience $\approx s/2$ photons worth of recoil heating, where s is the average number of photons scattered by an atom to get from $|{\uparrow}\rangle$ to $|{\downarrow}\rangle$ during the repumping process. In Fig. 25, we show how recoil heating can be reduced by coherently reinitializing most of the atoms into $|{\downarrow}\rangle$ using a microwave $\pi/2$ pulse before turning on the repumping.

The loss of contrast ϵ due to dephasing during the Ramsey evolution time is assumed to be small for the results presented in this section to be valid. Dephasing causes the off-diagonal elements of the density matrix representing the state of the ensemble to decay, resulting in a mixed state. The mixed state can be regarded as a tensor product of a pure state representing a smaller ensemble of size $N(1-\epsilon)$ atoms in a coherent superposition of $|{\uparrow}\rangle$ and $|{\downarrow}\rangle$ [Fig. 25(a)], with pure states representing the decohered atoms with $\epsilon N/2$ atoms collapsed in $|{\uparrow}\rangle$ and $|{\downarrow}\rangle$ on average. The QND readout causes an additional $(1-p)M_s$ atoms to collapse into $|{\uparrow}\rangle$ and pM_s atoms to collapse into $|{\downarrow}\rangle$, provided $m_s = M_s/N \ll 1$. Following a microwave $\pi/2$ pulse that rotates most of the atoms into $|{\downarrow}\rangle$, we find that approximately $s(m_s+\epsilon)/2$ photon recoils per atom is required to reinitialize the entire ensemble into $|{\downarrow}\rangle$. The contribution from quantum backaction into J_y is of order sm_s/Nm_s^{proj} and may be safely ignored for small spectroscopic enhancements.

(a) Atomic spin state after QND measurement:

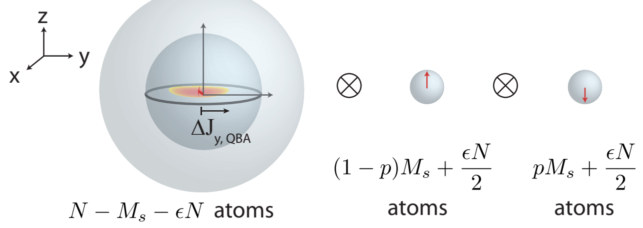
z
y
x
$\Delta J_{y,\text{QBA}}$
$\otimes$
$\otimes$
$N - M_s - \epsilon N$ atoms
$(1-p)M_s + \frac{\epsilon N}{2}$ atoms
$pM_s + \frac{\epsilon N}{2}$ atoms

(b) After π/2-rotation about y:

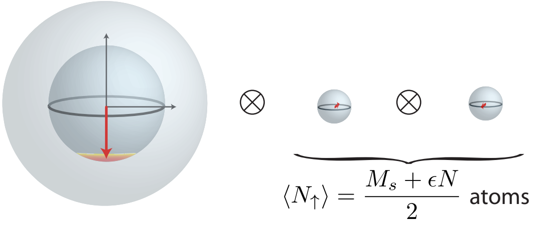
$\otimes$
$\otimes$
$\langle N_\uparrow \rangle = \frac{M_s + \epsilon N}{2}$ atoms

(c) After repumping:

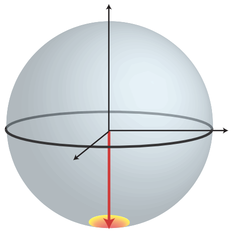

FIG. 25. (Color online) Coherent reinitialization scheme to reduce photon recoil heating in a complete experimental cycle. (a) Dephasing during the Ramsey evolution can be described as a shrinking of the coherent part of the Bloch vector from length $N/2$ to length $N(1-\epsilon)$, where $\epsilon \ll 1$ characterizes the amount of dephasing. The dephased atoms can be represented as if they had collapsed into $|{\uparrow}\rangle$ and $|{\downarrow}\rangle$ with $\epsilon N/2$ atoms in each state. Performing a QND readout with $m_s = M_s/N \ll 1$ results in further shrinkage of the coherent Bloch vector and additional collapse of the atoms. (b) Performing a microwave $\pi/2$ pulse about $\hat{y}$ rotates the coherent Bloch vector to the south pole and the collapsed atoms onto the equator of the Bloch sphere. (c) Applying optical repumping beams reinitializes the ensemble to the south pole, with the photon recoil heating arising from repumping the atoms in superposition states into $|{\downarrow}\rangle$. The contribution arising from the quantum backaction of repumping back into a CSS is negligible provided the spectroscopic enhancement is small compared to the Heisenberg limit.

In summary, we have shown that it is possible to impart only $s(m_s+\epsilon)/2$ optical photon recoils per atom through the coherent reinitialization scheme, as opposed to the much larger $s/2$ recoils per atom without coherent reinitialization. Note the reason why the scheme works is because we have traded optical photon recoils with microwave photon recoils, which impart recoil energy ~ 8 orders of magnitude smaller than that of optical photons. If an optical transition separated $|{\uparrow}\rangle$ from $|{\downarrow}\rangle$, such as in optical lattice clocks, the scheme presented would not reduce recoil heating substantially.

IX. CONCLUSIONS

In conclusion, we have presented detailed expressions for how cavity-aided nondemolition measurements of atomic populations scale with key experimental parameters: cavity linewidth, cavity geometry, collective cooperativity, and Raman transition probabilties. This analysis will be important in future experiments for reducing photon-recoil heating and for producing highly entangled states with enhanced spectroscopic sensitivities relative to the SQL. We have given experimental details for two different probing schemes in ^{87}Rb and estimated fundamental limits on conditional spin-squeezing in ensembles of ^{87}Rb atoms. We expect that this analysis will guide future experimental efforts on squeezing on a cycling transition, specifically in ^{87}Rb and can be straightforwardly adapted to other atoms with ground state hyperfine structure such as Cs and other alkali elements used in spectroscopy and quantum information experiments.

X. ACKNOWLEDGEMENTS

This work was supported in parts by NIST, the NSF PFC, ARO, and DARPA QUASAR. Z.C. was supported in part by A*STAR Singapore. J.G.B. acknowledges support from NSF GRF, and K.C.C. acknowledges support from NDSEG.

[1] Z. Chen, J. G. Bohnet, S. R. Sankar, J. Dai, and J. K. Thompson, Phys. Rev. Lett. **106**, 133601 (2011).

[2] J. Kitching, S. Knappe, and E. A. Donley, IEEE Sensors Journal **11**, 1749 (2011).

[3] V. Meyer, M. A. Rowe, D. Kielpinski, C. A. Sackett, W. M. Itano, C. Monroe, and D. J. Wineland, Phys. Rev. Lett. **86**, 5870 (2001).

[4] D. Leibfried, M. D. Barrett, T. Schaetz, J. Britton, J. Chiaverini, W. M. Itano, J. D. Jost, C. Langer, and D. J. Wineland, Science **304**, 1476 (2004).

[5] J. Estève, C. Gross, A. Weller, S. Giovanazzi, and M. K. Oberthaler, Nature **455**, 1216 (2008).

[6] J. Appel, P. J. Windpassinger, D. Oblak, U. B. Hoff, N. Kjrgaard, and E. S. Polzik, Proc. Nat. Acad. Sci. **106**, 10960 (2009).

[7] M. H. Schleier-Smith, I. D. Leroux, and V. Vuletić, Phys. Rev. Lett. **104**, 073604 (2010).

[8] C. Gross, T. Zibold, E. Nicklas, J. Estève, and M. K. Oberthaler, Nature **464**, 1165 (2010).

[9] M. F. Riedel, P. Böhi, Y. Li, T. W. Hänsch, A. Sinatra, and P. Treutlein, Nature **464**, 1170 (2010).

[10] B. Lücke, M. Scherer, J. Kruse, L. Pezzé, F. Deuretzbacher, P. Hyllus, O. Topic, J. Peise, W. Ertmer, J. Arlt, L. Santos, A. Smerzi, and C. Klempt, Science **334**, 773 (2011).

[11] R. J. Sewell, M. Koschorreck, M. Napolitano, B. Dubost, N. Behbood, and M. W. Mitchell, (2011), arXiv:1111.6969.

[12] C. D. Hamley, C. S. Gerving, T. M. Hoang, E. M. Bookjans, and M. S. Chapman, Nature Phys. **8**, 305 (2012).

[13] J. Lodewyck, P. G. Westergaard, and P. Lemonde, Phys. Rev. A **79**, 061401 (2009).

[14] D. B. Hume, T. Rosenband, and D. J. Wineland, Phys. Rev. Lett. **99**, 120502 (2007).

[15] D. J. Wineland, J. J. Bollinger, W. M. Itano, and D. J. Heinzen, Phys. Rev. A **50**, 67 (1994).

[16] I. D. Leroux, M. H. Schleier-Smith, and V. Vuletić, Phys. Rev. Lett. **104**, 073602 (2010).

[17] P. Grangier, J. A. Levenson, and J.-P. Poizat, Nature **396**, 537 (1998).

[18] S. Chaudhury, G. A. Smith, K. Schulz, and P. S. Jessen, Phys. Rev. Lett. **96**, 043001 (2006).

[19] Y. Takahashi, K. Honda, N. Tanaka, K. Toyoda, K. Ishikawa, and T. Yabuzaki, Phys. Rev. A **60**, 4974 (1999).

[20] T. Takano, M. Fuyama, R. Namiki, and Y. Takahashi, Phys. Rev. Lett. **102**, 033601 (2009).

[21] A. Kuzmich, N. P. Bigelow, and L. Mandel, Europhys. Lett. **42**, 481 (1998).

[22] L. K. Thomsen, S. Mancini, and H. M. Wiseman, J. Phys. B: At. Mo. Opt. Phys. **35**, 4937 (2002).

[23] J. Geremia, J. K. Stockton, A. C. Doherty, and H. Mabuchi, Phys. Rev. Lett. **91**, 250801 (2003).

[24] L. B. Madsen and K. Mølmer, Phys. Rev. A **70**, 052324 (2004).

[25] K. Mølmer and L. B. Madsen, Phys. Rev. A **70**, 052102 (2004).

[26] A. Kuzmich and T. A. B. Kennedy, Phys. Rev. Lett. **92**, 030407 (2004).

[27] M. Auzinsh, D. Budker, D. F. Kimball, S. M. Rochester, J. E. Stalnaker, A. O. Sushkov, and V. V. Yashchuk, Phys. Rev. Lett. **93**, 173002 (2004).

[28] J. J. Hope and J. D. Close, Phys. Rev. Lett. **93**, 180402 (2004).

[29] J. K. Stockton, R. van Handel, and H. Mabuchi, Phys. Rev. A **70**, 022106 (2004).

[30] J. J. Hope and J. D. Close, Phys. Rev. A **71**, 043822 (2005).

[31] S. R. de Echaniz, M. W. Mitchell, M. Kubasik, M. Koschorreck, H. Crepaz, J. Eschner, and E. S. Polzik, J. Opt. B: Quantum Semiclass. Opt. **7**, S548 (2005).

[32] I. H. Deutsch and P. S. Jessen, Opt. Comm. **283**, 681 (2010).

[33] A. Kuzmich, L. Mandel, J. Janis, Y. E. Young, R. Ejnisman, and N. P. Bigelow, Phys. Rev. A **60**, 2346 (1999).

[34] A. Kuzmich, L. Mandel, and N. P. Bigelow, Phys. Rev. Lett. **85**, 1594 (2000).

[35] P. J. Windpassinger, D. Oblak, U. B. Hoff, J. Appel, N. Kjrgaard, and E. S. Polzik, New J. Phys. **10**, 053032 (2008).

[36] W. Wasilewski, K. Jensen, H. Krauter, J. J. Renema, M. V. Balabas, and E. S. Polzik, Phys. Rev. Lett. **104**, 133601 (2010).

[37] M. Koschorreck, M. Napolitano, B. Dubost, and M. W. Mitchell, Phys. Rev. Lett. **104**, 093602 (2010).

[38] M. Koschorreck, M. Napolitano, B. Dubost, and M. W. Mitchell, Phys. Rev. Lett. **105**, 093602 (2010).

[39] V. Shah, G. Vasilakis, and M. V. Romalis, Phys. Rev. Lett. **104**, 013601 (2010).

[40] S. Li, P. Vachaspati, D. Sheng, N. Dural, and M. V. Romalis, Phys. Rev. A **84**, 061403 (2011).

[41] J. Ye, L.-S. Ma, and J. L. Hall, J. Opt. Soc. Am. B **15**, 6 (1998).

[42] I. Teper, Y.-J. Lin, and V. Vuletić, Phys. Rev. Lett. **97**, 023002 (2006).

[43] A. E. B. Nielsen and K. Mølmer, Phys. Rev. A **77**, 063811 (2008).

[44] I. Teper, G. Vrijsen, J. Lee, and M. A. Kasevich, Phys. Rev. A **78**, 051803 (2008).

[45] S. Bernon, T. Vanderbruggen, R. Kohlhaas, A. Bertoldi, A. Landragin, and P. Bouyer, New J. Phys. **13**, 065021 (2011).

[46] H. Zhang, R. McConnell, S. Ćuk, Q. Lin, M. H. Schleier-Smith, I. D. Leroux, and V. Vuletić, Phys. Rev. Lett. **109**, 133603 (2012).

[47] H. Tanji-Suzuki, I. D. Leroux, M. H. Schleier-Smith, M. Cetina, A. T. Grier, J. Simon, and V. Vuletic, in *Advances in Atomic, Molecular, and Optical Physics*, Vol. 60, edited by E. Arimondo, P. R. Berman, and C. C. Lin (Academic Press, 2011) pp. 201 – 237.

[48] J. H. Wesenberg, A. Ardavan, G. A. D. Briggs, J. J. L. Morton, R. J. Schoelkopf, D. I. Schuster, and K. Mølmer, Phys. Rev. Lett. **103**, 070502 (2009).

[49] I. Diniz, S. Portolan, R. Ferreira, J. M. Gérard, P. Bertet, and A. Auffèves, Phys. Rev. A **84**, 063810 (2011).

[50] M. Albert, J. P. Marler, P. F. Herskind, A. Dantan, and M. Drewsen, Phys. Rev. A **85**, 023818 (2012).

[51] T. Holstein and H. Primakoff, Phys. Rev. **58**, 1098 (1940).

[52] C. W. Gardiner and M. J. Collett, Phys. Rev. A **31**, 3761 (1985).

[53] Y. Zhu, D. J. Gauthier, S. E. Morin, Q. Wu, H. J. Carmichael, and T. W. Mossberg, Phys. Rev. Lett. **64**, 2499 (1990).

[54] The approximation that the single-particle decay rate Γ into all modes other than the cavity mode holds true in the limit that the cavity subtends a small fraction of the total solid angle as seen by the atom [61].

[55] R. E. Kalman, Transactions of the ASME–Journal of Basic Engineering **82**, 35 (1960).

[56] J. G. Bohnet, Z. Chen, J. M. Weiner, K. C. Cox, and J. K. Thompson, (2012), arXiv:1208.1710, Supporting Online Material.

[57] J. J. . Bollinger, W. M. Itano, D. J. Wineland, and D. J. Heinzen, Phys. Rev. A **54**, R4649 (1996).

[58] M. J. Holland and K. Burnett, Phys. Rev. Lett. **71**, 1355 (1993).

[59] H. Uys, M. J. Biercuk, A. P. VanDevender, C. Ospelkaus, D. Meiser, R. Ozeri, and J. J. Bollinger, Phys. Rev. Lett. **105**, 200401 (2010).

[60] M. Saffman, D. Oblak, J. Appel, and E. S. Polzik, Phys. Rev. A **79**, 023831 (2009).

[61] H. J. Kimble, Physica Scripta **1998**, 127 (1998).